Numerical investigation of broadband trailing edge noise through large eddy simulations

Rubens Dellepiane

Dipartimento di Ingegneria Meccanica, Energetica, Gestionale e
dei Trasporti (DIME)
and
Linnè FLOW Centre (KTH)

University of Genova

Supervisors

Alessandro Bottaro, Ardeshir Hanifi, Zhenyang Yuan

In partial fulfillment of the requirements for the degree of

Ingegneria Meccanica, Energia e Aeronautica

March 26th, 2024

Acknowledgements

In Italiano, per tutti quelli che hanno portato qualcosa di bello nella

mia vita, la Famiglia e gli Amici.

In English, for who made all this work possible, sharing his

knowledge, his comprehension and, last but not least, his codes:

谢谢 Zhenyang!

In Spanish, Croatian, French, Chinese, Japanese, Swedish, Indian, Iranian for who made my stay in

Stockholm unforgettable: Gracias, Hvala, Merci, 谢谢, ありがとう, Tack, धन्यवाद, ممنون

Abstract

Sommario in Italiano

Con il seguente studio, si riporta l'attività di ricerca su un'ala 3D con profilo aerodinamico NACA0012, svolta per comprendere meglio la generazione di rumore dal bordo d'uscita del profilo alare e, in futuro, come controllarlo e mitigarlo.

Sono state effettuate due simulazioni numeriche (large eddy simulations o LES), con $Re = 200'000$ e $M = 0,3$ (numero di Reynolds basato sulla corda e numero di Mach basato sulla velocità del flusso indisturbato), una con iniezione di free stream turbulence (FST) in prossimità del bordo d'attacco dell'ala e una con un semplice flusso completamente laminare prima del modello. Per l'oggetto studiato, le condizioni imposte di Mach e Reynolds dovrebbero portare a un trailing edge noise a banda larga e questo è coerente con l'analisi spettrale effettuata su diverse sonde posizionate nello span dell'ala a $\frac{x}{c} = 88\%$ e $\frac{x}{c} = 92\%$, che mostrano una "gobba" nella power spectral density (PSD) del segnale di pressione. Infine, evidenziamo che l'iniezione di FST prima del bordo d'attacco influisce sull'aerodinamica, in quanto i coefficienti di pressione e di attrito cambiano profondamente, ma è meno evidente per quanto riguarda l'acustica, eccezion fatta per i modi provenienti dalla Spectral Proper Orthogonal Decomposition (SPOD), che per il caso con iniezione di FST mostrano una sorgente

di rumore non fisica situata nella zona di iniezione stessa.

I campi di flusso e acustica calcolati sono stati confrontati con gli esperimenti eseguiti presso la TU Berlin [1].

Abstract in English

Here, we report the results of our simulations of the flow filed around a 3D wing with a NACA0012 profile. The aim of our work has been to better understand the noise generation mechanisms at the wing trailing edge. This knowledge can further be used to design efficient noise control devices.

Two sets of large-eddy simulations (LES) have been performed with $Re = 200'000$ and $M = 0.3$ (chord length-based Reynolds number and free stream velocity-based Mach number, respectively), one with fully laminar free stream and another with the free-stream turbulence (FST) intensity of $Tu = 1\%$, generated by localized forcing near the leading edge of the wing. For the object studied here, the imposed flow conditions (Mach and Reynolds numbers) result in a broadband trailing-edge noise. The spectral analysis carried out at several probes located along the span of the wing at $\frac{x}{c} = 88\%$ and $\frac{x}{c} = 92\%$ show a hump in the power spectral density (PSD) of the pressure signal. We have observed that the forcing of FST prior to the leading edge affects the flow quantities over the wing and the pressure and friction coefficients change significantly. However, its effect on the acoustics field is not strong, with the exception of the area where the FST is generated. This region appears as a non-physical noise source in the Spectral Proper Orthogonal Decomposition (SPOD) modes.

The computed flow and acoustics fields has been compared with the

experiments performed at TU Berlin [1].

Contents

List of Figures

List of Tables

Chapter 1

Introduction

1.1 Motivations

The wind energy production is growing in importance nowadays, due to the increasing need of clean energy. With its developing, also studies on how to improve its engineering aspects are spreading out and the following thesis work is part of a bigger analysis on the generation of noise by the trailing edge of airfoils implemented in wind turbines' blades. The aim is to better understand the physics involved and, hopefully, find some future developments to reduce the noise spreading from on-shore wind farms, which is one of the main limiting conditions of the technology itself.

1.2 Context of the Study

As above specified, this work is part of an extensive project on wind turbines' noise generation, including experimental and numerical investigations, which involves the collaboration of KTH (Sweden), TUB (Germany) and ITA (Brazil). In this context, the following thesis places itself on the numerical simulations and

analyses of a NACA 0012 three-dimensional blade at six degrees angle of attack (AoA = 6°).

1.3 Objectives and Contributions

The main objective of this study is to match experimental data gathered on the same model at the University of Berlin[1] and extract useful additional information to better understand the problem of noise generation by the trailing edge. To accomplish this goal, two large eddy simulations (LES) had been set via the computational fluid dynamics (CFD) solver PyFR [4], an open source Python-based code.

1.4 Overview of the Thesis

On the following, different topics will be covered: the dissertation will start with some basic theory regarding fluid dynamics and noise generation (Chapter 2); Then, in Chapter 3 and 4 the mesh generation process and the simulation set-up will be analysed, respectively, for the two simulation cases:

- LES with no free stream turbulence, NACA 0012, AoA = 6°

- LES with free stream turbulence, Turbulence intensity level Tu = 1% , NACA 0012, AoA = 6°

For the latter simulation, a value of free stream turbulence intensity has been imposed via a PyFR plugin [4], to better match the experimental results. Chapter 5 will be used to introduce the results of each case and to compare them and, finally, the conclusions will be drown in Chapter 6.

---

[1]A big thank you to Simon Demange and Simon Jekosh for sharing their knowledge and their data. An interesting paper related to the same topic as the one studied here, but from the experimental side, can be found at [1].

Chapter 2

Background Theory

Summary

Here the main aspects of fluid dynamics and acoustics related to this work will be covered. The aim of this section is to recall useful background info, without the will of fully explaining the almost infinite theory related to the field of fluid mechanics.

2.1 Fluid Dynamics

This section will represent the needed basis for the main discussion, as we need to introduce some fundamental concepts used henceforth.

2.1.1 Compressible and incompressible Navier-Stokes equations

The first important thing that will be introduced is about the distinction between compressible and incompressible flows. Speaking qualitatively, a compressible flow distinguish itself from an incompressible one due to non negligible changes

3

in density. Taking into account the actual definition, an incompressible flow is the one which has a null velocity divergence.

The two definitions can be linked [5], as one can demonstrate that, for mass conservation:

$$\frac{d}{dt} \int_{\wp} \rho \, dV = 0 \qquad (2.1)$$

Where $\wp$ indicates the volume of fluid on which the integral is calculated.

From (2.1), using the transport theorem, we have:

$$\int_{\wp} (\frac{D\rho}{Dt} + \rho \nabla \cdot \mathbf{u}) \, dV = 0 \qquad (2.2)$$

Now, being $\wp$ an arbitrary volume, we have that:

$$\frac{D\rho}{Dt} + \rho \nabla \cdot \mathbf{u} = 0 \qquad (2.3)$$

and, considering that the density variation in time and space has to be null for an incompressible flow, we reach the statement that $\rho \nabla \cdot \mathbf{u} = 0$ and hence:

$$\nabla \cdot \mathbf{u} = 0 \qquad (2.4)$$

So (2.2) defines the continuity for a compressible flow, whereas (2.4) is referred to an incompressible one. This was an important first statement, that leads to the fundamentals of fluid mechanics: the Navier-Stokes momentum equations. Again, they can be defined for compressible and incompressible flows as follow:

$$\rho \frac{D\mathbf{u}}{Dt} = \rho(\frac{\partial \mathbf{u}}{\partial t} + \mathbf{u}(\nabla \cdot \mathbf{u})) = -\nabla p + \mu \nabla^2 \mathbf{u} + \frac{1}{3}\mu\nabla(\nabla \cdot \mathbf{u}) + \rho\mathbf{g} \qquad (2.5)$$

Valid in the most generic way, for compressible flows.

Taking into account incompressibility, (2.5) becomes:

$$\rho_0 \frac{D\mathbf{u}}{Dt} = \rho_0 (\frac{\partial \mathbf{u}}{\partial t} + \mathbf{u}(\nabla \cdot \mathbf{u})) = -\nabla p + \mu \nabla^2 \mathbf{u} + \rho_0 \mathbf{g} \tag{2.6}$$

with ρ_0 being the state constant density. In an engineering context, it is usually stated also that a flow can be considered as incompressible when the Mach number characterizing it, is $M \leq 0.3$

2.1.2 Turbulence

Another key point to understand what will follow is the definition of turbulence and what is related to it.

In fluid mechanics, we usually refer to "turbulence" when speaking about random fluctuations in the fluid velocity [6]. The problem is much more complicated than what it looks like from this definition and it has been an important field of research for many years now, and probably beeing so for many others to come. Anyways, one can simplify the problem subdividing the flow into two main components: the mean state and the fluctuations. If we look at the mean state as the average of the quantity of interest, we can define the problem as follows:

$$\alpha = \overline{\alpha} + \alpha' \tag{2.7}$$

Where $\overline{\alpha}$ stands for the average operated in time (and eventually space) and α' represents the turbulent fluctuations. Here α generalizes any of the quantities of interest, i.e. $\mathbf{u}$, p, μ etc.

One of the most important quantities related to this assumption is the turbulence intensity level, usually simply called Tu, which is the ratio between the root mean square of the velocity fluctuations and the free stream velocity:

$$Tu = \frac{\sqrt{\frac{1}{3}(\langle u'^2 \rangle + \langle v'^2 \rangle + \langle w'^2 \rangle)}}{\overline{\mathbf{u}}} \tag{2.8}$$

with $\langle \cdot \rangle$ defining the average in time and, eventually, space.
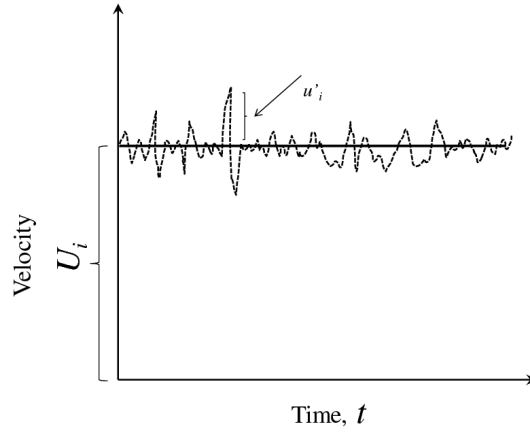
Figure 2.1: Velocity signal showing turbulent fluctuations in time

2.1.3 Stress tensor

The next theoretical argument will be about the stress tensor. The definition itself is included in the compressible Navier-Stokes momentum equation, but it is needed to better specify the tensor, as it will be used to define the skin friction coefficient, which will be introduced in the next paragraph. If we look at the stress tensor as:

$$\overrightarrow{\boldsymbol{\sigma}} = -p\overrightarrow{\mathbf{I}} + \overrightarrow{\boldsymbol{\tau}} \tag{2.9}$$

with p being the pressure, $\overrightarrow{\mathbf{I}}$ the identity matrix and $\overrightarrow{\boldsymbol{\tau}}$ the deviatoric part of the stress tensor, then recalling from equation (2.5), which is expressed in vectoral

6

form and can so be divided in three scalar equations, the term

$$\mu\nabla^2\mathbf{u} + \frac{1}{3}\mu\nabla(\nabla\cdot\mathbf{u})$$

can be seen as a simplification of $\vec{\vec{\tau}}$; we can then define it better as:

$$\vec{\vec{\tau}} = \mu(\nabla\mathbf{u} + (\nabla\mathbf{u})^T) + \lambda(\nabla\cdot\mathbf{u})\vec{\vec{\mathbf{I}}} \tag{2.10}$$

Where λ is the so called "volume viscosity" and it is proportional to the molecular viscosity μ, usually with a multiplication factor $-\frac{2}{3}$, so that $\lambda = -\frac{2}{3}\mu$. This being said, the discussion can go on with the next section, defining friction and pressure coefficients.

2.1.4 Skin friction coefficient and pressure coefficient

Here it will be discussed about two of the most important non dimensional values that will be taken into account in this thesis work: the pressure and the friction coefficients, also described as C_p and C_f. Both are essential to understand the characteristics of the flow itself and usually (as in this work, for example) they are the first variables to check to see if a good agreement between simulations and experiments is achieved.

2.1.4.1 C_f

The definition of the (skin) friction coefficient comes from the definition of the stress tensor. Considering that for Newtonian fluids we usually state that the wall shear stress is defined as:

$$\tau_{wall} = \mu \cdot \frac{du}{dy} \tag{2.11}$$

Which is valid for a 2-D flow and comes from the more general definition:

$$\tau_{wall} = \boldsymbol{\tau} \cdot \mathbf{t} \tag{2.12}$$

Where $\mathbf{t}$ is the normalized vector tangential to the profile and $\boldsymbol{\tau}$ the shear stress vector, which comes from the dot product of the shear stress tensor and the vector normal to the wall as:

$$\boldsymbol{\tau} = \vec{\vec{\tau}} \cdot \mathbf{n}$$

and introducing another definition of τ_{wall}, including C_f:

$$\tau_{wall} = p_{dyn} \cdot C_f \tag{2.13}$$

with p_{dyn} being the dynamic pressure $p_{dyn} = \frac{1}{2}\rho u_{inf}^2$; if we take into account equation (2.10), inverting equation (2.13) it is straightforward to get C_f.

2.1.4.2 C_p

Regarding the pressure coefficient, the definition is straightforward, as it is just a scaling of the pressure on the surface with the dynamic pressure:

$$c_p = \frac{p - p_{inf}}{p_{dyn}} \tag{2.14}$$

2.1.5 Law of the wall

In this section we will deal with other important definitions, in particular some dimensionless flow variables, which belong to the "law of the wall" theory. Looking deeper into this, one needs to refer to Prandtl's discovery about the dependency between velocity, density, viscosity, shear stress and distance from the wall [7].

In particular, taking into account the above mentioned quantities, it is possible to create two dimensionless groups, one correlated to the other:

$$u^+ = \frac{u}{u_\tau} \tag{2.15}$$

and

$$y^+ = \frac{y \rho u_\tau}{\mu} \tag{2.16}$$

With u_τ defining the "shear velocity" so that $u_\tau = \sqrt{\frac{\tau_{wall}}{\rho}}$.

Given these definitions, many scientists had tried in the years to find the exact relation between (2.15) and (2.16) in term of $u^+ = f(y^+)$ and many empiric formulations had been drown, but what is certain is that, starting from the wall and moving in the flow along the wall normal direction, one can identify different regions, each one characterized by different aspects, but always findable in disparate types of flow; this is why the law of the wall is one of the most important feedback about the goodness of an experimental or simulative campaign. A graph will be here reported, to better explain what had been written above and the related mathematical formulation for each region.
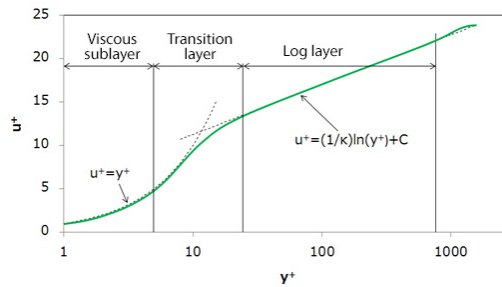
Figure 2.2: Law of the wall and boundary layer's zone definition [3]

In figure (2.2) the values of κ and C defining the log layer region, are empirical

and usually around:

$$\kappa = 0.4$$

$$C = 5$$

2.2 Acoustics

2.2.1 Useful Non-dimensional quantities

As one of the main points of this thesis work is to make comparisons between different numerical and experimental results, it is needed to refer everything to non-dimensional quantities, which can correctly identify the physics happening in a common problem which has different definitions, as experiments and simulations about the same case.

More specifically, as far as the acoustics are concerned, we will refer to the frequency domain and hence it is needed to introduce the Strouhal number (St), which represents a frequency non-dimensionalised with a characteristic length and a characteristic velocity. In the case here reported:

$$St = f \cdot \frac{c}{U} \tag{2.17}$$

With $f = \frac{1}{dt}$, dt being the sampling time step, c being the chord length and U being the free stream velocity.

Taking this into account, also the Helmoltz number will be further used, thanks to its relation with the Mach number, which enables us to compare experimental and numerical results obtained with different Mach conditions.

$$He = 2\pi St M \tag{2.18}$$

With M being the Mach number $M = \frac{u_{inf}}{a}$, u_{inf} the free stream velocity and a the speed of sound.

2.2.2 Scattering condition

As will be further investigated in paragraph 5.1.2, one of the most interesting things to study about this research, is the noise arising from the trailing edge, which is built up from the interaction between the airfoil itself and the pressure fluctuations resulting from the wake and turbulent boundary layer. It has to be underlined though that this mechanism happens only under some specified scattering conditions, which bring to propagative waves in the acoustic field: analysing the spanwise coherent structures, which are believed to have a great influence on the trailing edge noise [1], one can introduce the spanwise wave number

$$k_z^n = \frac{2\pi n}{L_z} \tag{2.19}$$

Theoretically, for a wing with infinite span, the scattering condition can be reached only if $k_z^n = \frac{2\pi n}{L_z} < \frac{2\pi f}{a} = k_0$. Thus, it can be derived that:

$$
\begin{aligned}
\frac{2\pi n}{L_z} &< \frac{2\pi f}{a} \\
\frac{n}{L_z} &< \frac{f}{a} \\
\frac{fc}{U} &> \frac{nc}{L_z M} \\
St &> St_n
\end{aligned}
\tag{2.20}
$$

with $St_n = \frac{nc}{L_z M}$.

Introducing the Helmoltz number as defined in equation (2.18), the scattering condition becomes:

$$St > \frac{nc}{L_z M} = St_n$$

$$He = 2\pi St M > \frac{2\pi nc M}{L_z M} \qquad (2.21)$$

$$He > \frac{2\pi nc}{L_z} = k_z^n c = He_n$$

This means that, given a certain frequency He, if $k_z < k_z^n$ (which corresponds to $St > St_n$ or $He > He_n$), then the nth wave number is propagative and brings to growing perturbations which affect the acoustic field and bring noise. Otherwise, the waves are evanescent [8].

Note that, since the span extension of the wing is the denominator of the spanwise wavenumber, this could be problematic mainly for numerical simulations which, due to their limited span width, will bring, eventually, to high wavenumbers and hence, difficult matching with the scattering condition.

This is obviously not a problem for experiments, where the the span width can be increased a lot.

Chapter 3

Meshing Process

Summary

This section will be assigned for the meshing process explanation. As will be better understood in the following part of the work, the mesh is specific for each study case. Nevertheless, it is important to highlight that every meshing process is done with the aim of perceiving a certain resolution and, as for the cases under analysis, a LES resolution is the target. That being said, a target value of wall $y^+ = 0.9$ had been imposed for every studied case. As will be also further understood in the next chapter, the whole thesis work is based on two simulations: both have, as argument, a NACA 0012 airfoil with rounded trailing edge (radius 0.4 mm) and chord length 100 mm, numerical twin of the model tested experimentally in an anechoic chamber of the technical acoustics department of the Technical University Berlin [1].

Both simulations were run with AoA = 6° and $Re = 2 \cdot 10^5$; the only difference in the run had been the level of free stream turbulence which, as will be seen, has an influence on the meshing process. Before inspecting the two cases, we can describe the meshing process as a step sequence:

1. Imposition of a target y^+ for the first node of the mesh, considering the profile's normal direction

2. Definition of Reynolds number (Re) for the case

3. Evaluation of C_f via a preliminary RANS or via potential flow solver (XFOIL [9])

4. Definition of τ_{wall} from equation (2.13)

5. Definition of $u_\tau = \sqrt{\frac{\tau_{wall}}{\rho}}$

6. Reversal of equation (2.16) to get $y_{firstnode} = \frac{y^+ \mu}{\rho u_\tau}$

In any case one has to take into account that, when elevating the mesh to a high order interpolation, each cell will be populated with many nodes, in a proportional way to the polynomial degree imposed. For instance, if the solution polynomial degree is 4, one needs to consider that each cell side will be discretized with 5 points. Then, when meshing, it will be needed to impose $\Delta s = 4y_{firstnode}$, where $y_{firstnode}$ is the target distance for the first mesh node from the wall and Δs the distance of the first layer before elevating the mesh to a higher polynomial degree. Here, an imposition of $y^+ = 0.9$ and a $C_f = 0.007$ (obtained from XFOIL), together with a fourth polynomial interpolation degree, led to a value $\Delta s = 4y_{firstnode} = 0.028$, value used as input in PointWise for the first layer in direction normal to the wall.

As far as both cases here analysed are 3D, it is needed to specify also the spacing in the streamwise and spanwise directions. For both the simulations the wing has a spanwise extension $L_z = 43.75$, so 43.75% of the chord length, which is quite a big value for a LES, considering that the computational cost increases with the number of elements inserted in the spanwise direction. However, this helps matching the experimental results, as the consequences of imposing periodic

boundary conditions at $\frac{z}{c} = 0\%$ and $\frac{z}{c} = -43.75\%$ are less relevant. For both cases, it had been chosen to have 141 elements in the spanwise direction and 512 on the streamwise section of the wing, resulting in $\Delta x_{avg} \approx 0.46 \approx 16 \cdot \Delta s$ (i.e. $x^+ \approx 14.45 \approx 16 y^+$) and $\Delta z = 0.3125 \approx 11 \cdot \Delta s$ (i.e. $z^+ \approx 9.8 \approx 11 y^+$). This is true, of course, only for the mesh blocks near the wing, where the flow needs to be solved with high accuracy.

For both cases the mesh has a farfield which extends twenty chord lengths upstream and downstream and it is square shaped. Outisde the interval $-20\% < \frac{x}{c} < 210\%$ & $-30\% < \frac{y}{c} < 25\%$ the mesh gets more and more coarse, as it's not relevant to accurately solve the flow there, but just to capture sound waves, which are resolved, in this case, up to $St \approx 100$.

3.1 Case without free stream turbulence, Tu = 0%

This paragraph will be dedicated to introduce the 3D mesh used for the simulation without free stream turbulence. Here, in figure (3.1) one picture of the mesh in the plane (x,y) is reported. The next figure (3.2) is just a zoom up to better visualize the profile.

As it is possible to see from figure (3.2), the mesh is composed of a mixture of structured and unstructured cells. Where one wants to have better resolution in the solution, structured mesh is needed, but as soon as the region becomes less important, it is better to use unstructured mesh with tetrahedral cells, to reduce the number of nodes and so the computational cost of the simulation. Note that, for example, on the suction side of the profile, going towards the trailing edge (TE), it is needed to increase the number of structured layers growing in the normal direction from the airfoil surface. This because the profile has a positive
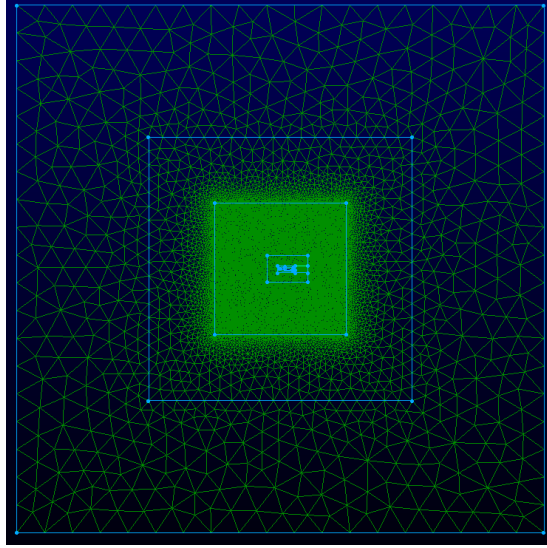
Figure 3.1: Mesh for LES without free stream turbulence
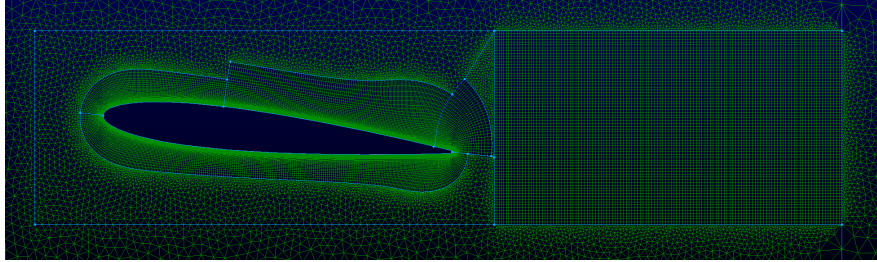
Figure 3.2: Mesh for LES without free stream turbulence, zoom-up

incidence angle, and this may cause a boundary layer separation on the suction side; anyways, even without separation, the physics characterizing the upper part of the airfoil are much more interesting than the ones happening on the lower side. For the mesh block starting near the leading edge (LE) and going down to the whole pressure side, we have 37 structured layers; for the intermediate block on the suction side, we have 42 structured layers and for the block near the TE on the suction side, we have 46 structured layers. For all the structured zones around the airfoil, there is a growing rate of 1.1 between one layer and the next one. The wake zone is constructed as a structured block with $\Delta x \approx \Delta y \approx 0.8$ and $\Delta z \approx 0.9$ (i.e. $x^+ \approx 25$, $y^+ \approx 25$ and $z^+ \approx 28$) and this results in a $50 \times 70 \times 126$

elements block. Considering that the wing block and the wake block have a different number of elements alongside z (respectively 141 and 50), it had been needed to connect them with an unstructured block. The shape of this block could seem "strange", but it comes from a series of attempts to overcome the limitation that PyFR has concerning the impossibility of using curved pyramid cells.

After the elevation to the 4th polynomial order, the grid consists in 483'037'555 degrees of freedom.

3.2 Case with free stream turbulence, Tu = 1%

As far as a turbulence injection in the free stream is concerned, there is no need in changing anything in the farfield of the mesh. The only thing that one needs to adjust is the mesh refinement in the injection zone, to fully capture the turbulent structures that will populate the region of the free stream where you want to perturb the base flow with turbulent fluctuations. To better understand this, refer to the appendix (A) which includes an explanation about how turbulence is generated in PyFR.

As it is possible to see from figure (3.3) and its zoom-up (fig. (3.4)), in front of the leading edge there is one structured block extending from $\frac{x}{c} = -20\%$ till the airfoil surface (the nose of the airfoil is located at $(x = -0.52, y = 1.03)$ with full span extension and within the interval $-7.4\% < \frac{y}{c} < 10.4\%$. This block has 36 elements alongside x ($\Delta x \approx 0.4$, $x^+ \approx 12.5$), 37 alongside y ($\Delta y \approx 0.5$, $y^+ \approx 15.7$) and 141 alongside z ($\Delta z = 0.3125$, $z+ \approx 9.8$). This block has been added to properly inject turbulence in the domain and carry it correctly towards the profile. The injection plane imposed in PyFR had these characteristics: plane normal to x-axis, with $\frac{x_{origin}}{c} = -18\%$, $-7.35\% < \frac{y}{c} < 10.35\%$ and $-43.75\% < \frac{z}{c} < 0\%$.
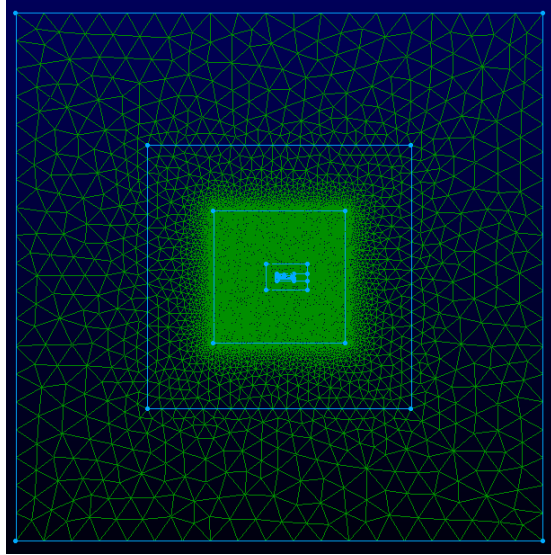
Figure 3.3: Mesh for LES with free stream turbulence, $Tu = 1\%$
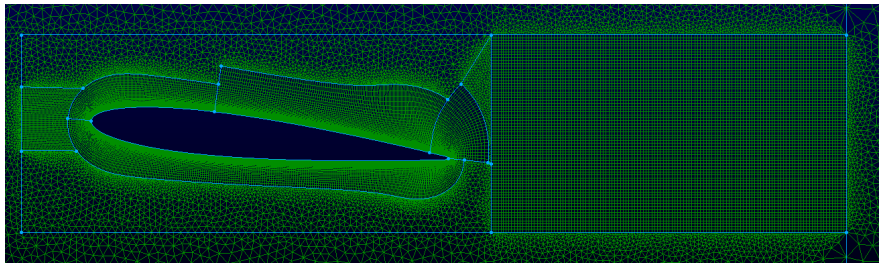
Figure 3.4: Mesh for LES with free stream turbulence, $Tu = 1\%$, zoom-up

After the elevation to the 4th polynomial order, the grid consists in 511'977'480 degrees of freedom.

Chapter 4

Case set-ups

Summary

Here we will discuss about the case set-up and the configuration files used in PyFR. Note that the set-up is exactly the same for both simulations, with the only exception of the turbulence plugin used for the simulation with $Tu = 1\%$. So, the explanation in paragraph (4.1) will be valid for both simulations. Something more about the set-up with free stream turbulence will be said in paragraph (4.2).

4.1 General case set-up

The software specific configurations will not be explored here, but we will focus on the physical problem.

The problem has been configured to be dimensionless and normalized in some key parameters. These are the main settings (we underline once more that the values will be reported without units of measure, since the solver works non-dimensionally; dimensionally, everything is consistent with the international system):

- Chord length $c = 100$

- Sound speed $a_{inf} = 1$

- Density $\rho_{inf} = 1$

- Mach number $M = 0.3$

- Reynolds number $Re = 2 \cdot 10^5$

- $\gamma = \frac{c_p}{c_v} = 1.4$ with c_p specific heat in constant pressure and c_v specific heat in constant volume

- Free stream velocity $\boldsymbol{u_{inf}} = (u_{inf}, v_{inf}, w_{inf}) = (0.3, 0, 0)$

- Pressure $p_{inf} = \frac{a_{inf}^2 \rho_{inf}}{\gamma} = 0.71$

- Energy $E_{inf} = \frac{p_{inf}}{\gamma - 1} + \frac{1}{2}\rho_{inf}(u_{inf}^2 + v_{inf}^2 + w_{inf}^2) = 1.83$

- Dynamic viscosity $\mu = \frac{\rho_{inf} u_{inf} c}{Re} = 0.00015$

- Prandtl number $Pr = 0.72$

In addition, the Sutherland law for viscosity had been used, imposing

$$c_p T_{ref} = \frac{\gamma}{\gamma - 1}\frac{p_{inf}}{\rho_{inf}} = 2.5 \tag{4.1}$$

With $T_{ref} = 293.15K$ and

$$c_p T_s = c_p T_{ref}\frac{T_s}{T_{ref}} = 0.94 \tag{4.2}$$

With $T_s = 110.9K$

As one of the main interests of this work is to study sound waves, it is important also to avoid reflections coming from the outlet region. To be sure about this, in the region with $x \in (1500, 2000)$, $y \in (-2000, 2000)$ and $z \in (-43.75, 0)$ a

"sponge" has been introduced via PyFR with a source term formulation, considering that, for continuity we have $\frac{\partial \rho}{\partial t} + \frac{\partial \rho u_i}{\partial x_i} = S = -(\rho - \rho_{ref})\sigma$. Physically one should have the term $S = 0$, but we are now modifying the outflow such that the imposition of Riemann invariant boundary condition and no reflections are achieved at the outlet of the domain, and this is done by tuning the term σ. Both simulations had been running going through a first transient part where the flow had to set up, going from the inlet to the outlet and stabilizing in term of pressure and velocity fluctuations over the airfoil. This first transient part had been solved with a second degree polynomial order and took approximately 36 convective time units (CTU), defined as $CTU = t\frac{u_{inf}}{c}$ where t is the actual simulation time and c is the chord length; for this transient part, the flow had been solved with an adaptive time step initially set to $dt = 0.002$ and a Runge-Kutta 45 time integrator scheme with PI controller. After the transient had been considered finished, the simulation had been switched to a 4th polynomial order with $dt = 0.00125$ and Total Variation Diminishing (tvd) Runge-Kutta 3 integration scheme, that had been running for 6 CTUs before starting collecting snapshots, in order to let numerical noise, coming from the change in polynomial solution order, vanish. After this two steps, snapshots had been collected with a sampling rate of 0.2 Hz (one snapshot every 0.015 CTUs). For the acoustics, and to match experimental data from TUB, several probes had also been added to the solution field; on these probes, the sampling frequency had been set to 0.8 Hz.

For the quadrature points populating each element of the mesh, a quadrature degree higher than the solution order had always been imposed, aiming to have more points where the integration of the flow equations could be done, than actual solution points. This could theoretically bring error, since some points are not resolved, but this is avoided using an anti-aliasing filter applied to the solver. As far as the boundary conditions are concerned, Riemann invariants had been

imposed on the boundary regions (inlet, outlet, free stream) and a no-sleep adiabatic boundary condition had been imposed on the wall.

4.2   Set-up for free stream turbulence simulation

As already said in the previous paragraph, most of the configurations are the same for both simulations. The only exception is for the turbulence plugin (see appendix A), introduced with the following configurations:

- $\rho_{avg} = 1$

- $u_{avg} = 0.3$

- $M_{avg} = 0.3$

- $Tu = 1\%$

- Turbulence length scale $TLS = 1(mm)$

- $\sigma = 0.7$

- Injection plane center $O = (-18, 1.5, -21.875)$

- Injection plane y-side length 17.7 (mm)

- Injection plane z-side length 43.75 (mm)

- Rotation axis for the injection plane: (0, 0, 1)

- Rotation angle 0° (injection plane normal to the streamwise direction)

Finally, we report that the simulation without free stream turbulence required about 24 days of run on 80 GPUs, whilst about 20 days of run on 120 GPUs had been reserved for the case with FST injection.

With the next chapter, the results from both simulations will be introduced and commented.

Chapter 5

Results and Comparisons

Summary

In this section it will be discussed about the numerical results from the large eddy simulations with and without free stream turbulence, making also comparisons with experimental data for the case under analysis.

5.1 Case without free stream turbulence

Everything that will be commented in the paragraphs included into this section, will regard the results coming from the LES done without free stream turbulence.

5.1.1 Flow field

Firstly, we will focus on analyzing the hydrodynamic field, before moving to the acoustic field in section 5.1.2.

5.1.1.1 Wall quantities and boundary layer velocity profiles

In this section it will be reported about the wall quantities introduced theoretically in 2.1.5 and also about the boundary layer velocity profiles in different stations alongside the streamwise airfoil coordinate.
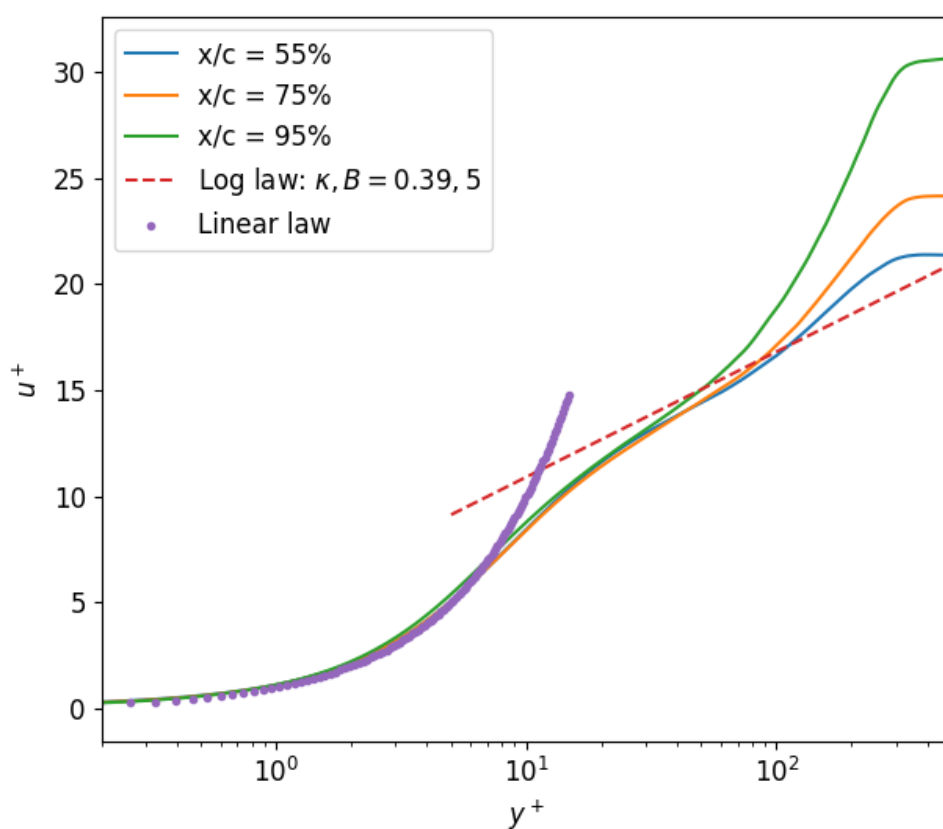
Figure 5.1: Law of the wall.

In figure (5.1) it is visible the behaviour of non-dimensional wall quantity u^+ as a function of y^+. The trend is consistent with the linear law near the wall and with the logarithmic law far from it. At $y^+ \geq 200$ the curve reaches a plateau since the velocity doesn't change anymore outside the boundary layer. As it can be seen in the picture, the maximum u^+ at fixed y^+ grows as the station moves

downstream. This can be explained considering that at high values of y^+ the flow velocity has become almost constant, hence the ratio $u^+ = \frac{u}{u_\tau}$ can grow only if u_τ decreases, and this is consistent with the fact that, downstream, the flow near the wall tends to be separated, and this results in a lower value of τ_{wall} and, consequently, of u_τ.
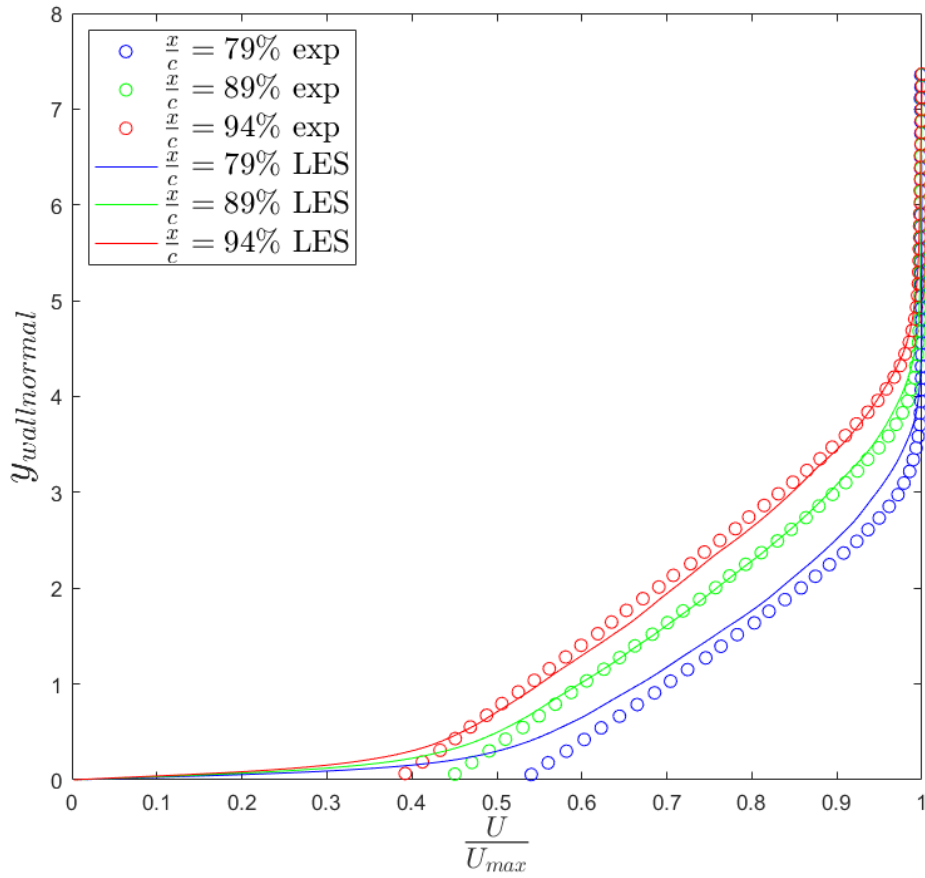
Figure 5.2: Boundary layer normalized velocity profiles.

In figure (5.2), the velocity profiles at different measuring stations alongside the profile are shown. Considering the high degree of uncertainty that is present in experimental results, since it is not possible to know with great precision where the wall effectively is and considering also the extreme thinness of the

boundary layer, the matching between LES and experiments is quite satisfying. It has to be specified that, to have a proper comparison, each profile had been obtained normalizing the velocity values with their maximum inside each profile. Besides, as for experiments, the profiles just show the magnitude in absolute value of the velocity, so U in the plots had been obtained from LES dataset as $U = \sqrt{u^2 + v^2 + w^2}$ for each solution point.

5.1.1.2 C_p

As far as the pressure coefficient is concerned, a comparison with experimental data is crucial to understand if the hydrodynamics coming from the simulation match with the hydrodynamics in the experiments. To do this evaluation, the numerical and experimental C_p distributions are reported in figure (5.3). For the numerical data, the C_p distribution comes from the time averaging and analysis of 1500 snapshots, which covers 22.5 CTUs.

As it can be seen from figure (5.3), the overall C_p distribution is good, considering also the Mach difference between experiments ($M = 0.089$) and simulation ($M = 0.3$), which certainly has an influence, but there is a significant shift in the position where the pressure coefficient experiences a drop on the suction side: this surely happens due to a laminar separation bubble that shows itself right after the leading edge. For the hydrodynamics and transition studies, it is important to capture numerically as accurately as possible the position of this bubble, as it has a strong influence on the transition from laminar to turbulent flow and this changes deeply the boundary layer characteristics downstream, affecting all the aerodynamic properties as drag and lift.

We have to underline that the above mentioned quantities are not of interest for the present work, as the main focus is on acoustics, but in order to have a more accurate simulation, also suitable for future investigations on different topics, a
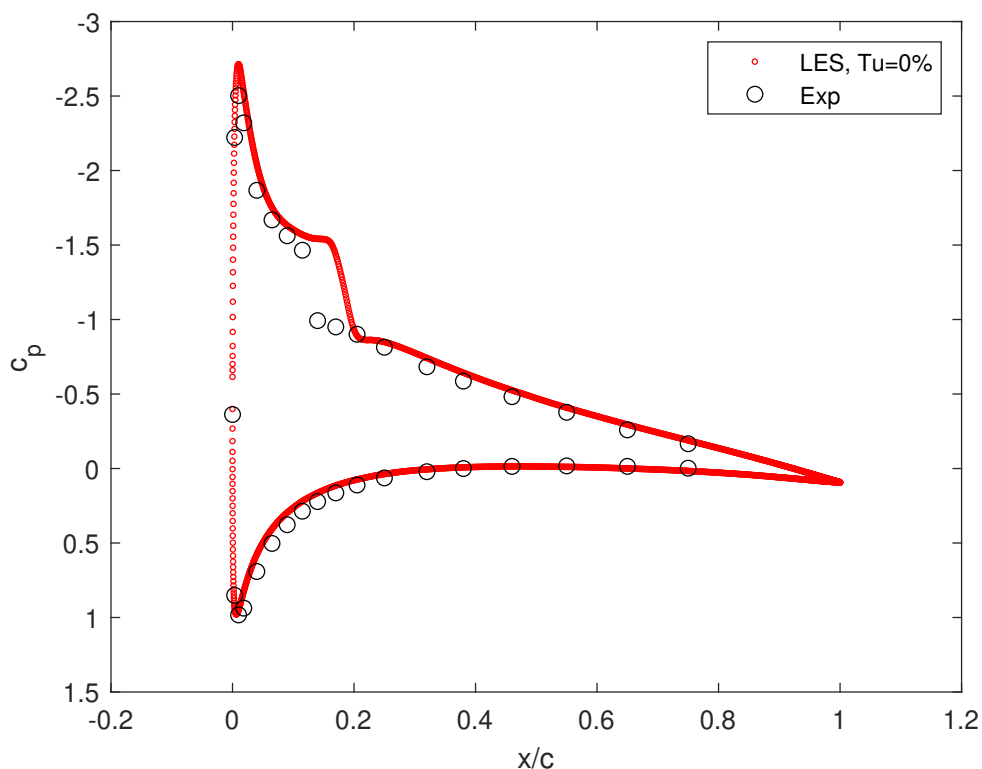
Figure 5.3: Pressure coefficient distribution coming from experimental campaign (black dots) and LES without FST (red dots). Pay attention to the sign of C_p in the y-axis: the graph had been inverted to show the C_p from suction side on the upper part and the one from pressure side on the lower part of the plot.

level of free stream turbulence had been added in the other case here presented, in order to better capture the position of the above mentioned laminar separation bubble: the results from it will be shown in paragraph 5.2.1.2.

5.1.1.3 C_f

To have a look also on the transition study of the simulated airfoil, it is also necessary to report the skin friction coefficient distribution.

In figure (5.4) only the C_f distribution over the suction side of the airfoil is reported, as it is on that side that the most interesting physics, concerning
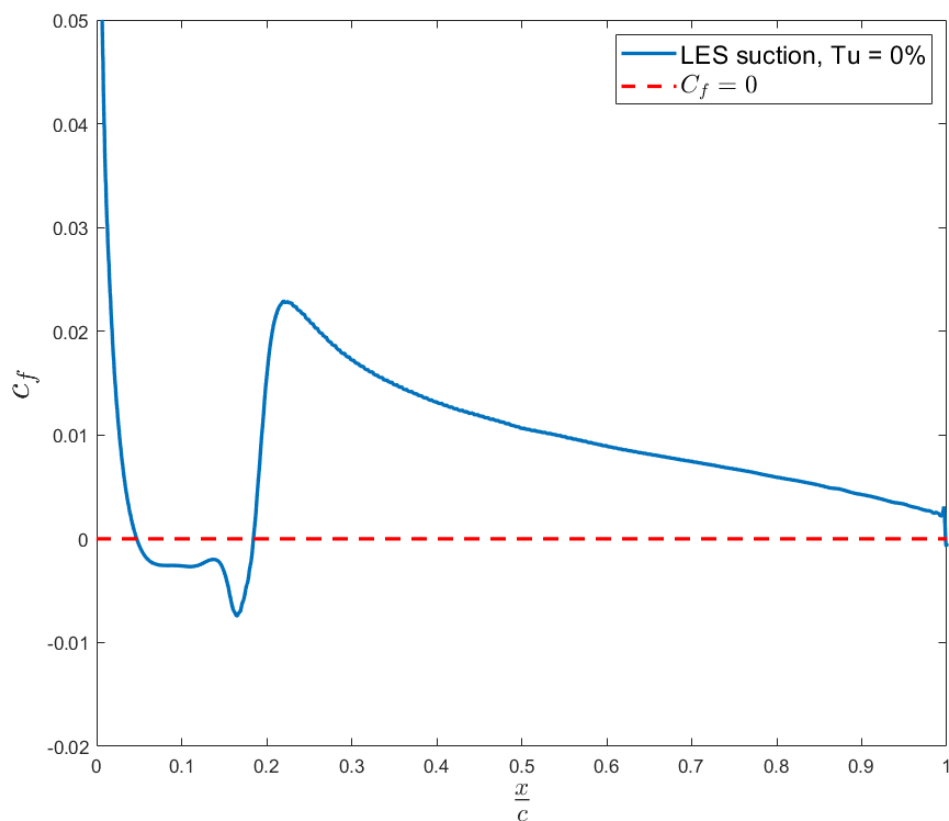
Figure 5.4: Skin friction coefficient for the LES without free stream turbulence; results from 1500 span-averaged snapshots, covering 22.5 CTUs

transition, happen.

It is easily visible that, for a certain percentage of profile chord (from $\frac{x}{c} = 4.7\%$ to $\frac{x}{c} = 18.4\%$) the C_f curve assumes negative values: this is the witness for the presence of a laminar separation bubble. It is also interesting to see where the transition happens; usually, the transition point is evaluated as the one where the C_f distribution experiments a sudden drop [10]: for the case under analysis, the mentioned point is located at $\frac{x}{c} = 14\%$. In paragraph 5.2.1.3 it will be reported also about the results for the simulation with free stream turbulence, underlining the main differences.

5.1.2 Acoustic field

5.1.2.1 Scattering condition

As stated in 2.2, it can be interesting to study the acoustics related to the pressure fluctuations on the surface of the airfoil, generated from the turbulence being present in its boundary layer and wake, and to better understand how this can bring to a scattering condition for the trailing edge noise generation, consisting in more than one wave number being propagative for the acoustic waves. As a starting point for this analysis, we begin studying the spectrum which shows the power spectral density of the pressure signals evaluated by single probes positioned at midspan on the airfoil suction side surface at $\frac{x}{c} = 88\%$ and $\frac{x}{c} = 92\%$, which correspond to the MEMS probes in the experimental setup [1], as well as the pressure signals from single probes situated at midspan in the acoustic field at $\frac{x}{c} = 1$ and $\frac{y}{c} = [+3, +1, -1]$. As it can be seen in image (5.5)(b), a peak can be seen in the acoustic pressure PSD at almost every scattering condition, and this is a witness for the goodness of the definition (2.20). Looking at figure (5.5)(a), the most interesting thing is the hump that shows itself around $St \approx 10$, underlining a good agreement with the experimental results. Also, concerning the spectra from the probes in the acoustic field, there is a good agreement with experimental data, exception made for the low frequencies, where the side plates used in the experimental setup [1] are believed to have an influence. Note that to match experimental and numerical results, it is needed to scale the acoustics with the Mach ratio $(\frac{Ma_{exp}}{Ma_{LES}})$ elevated to the fifth power, and the hydrodynamics with the dynamic pressure [8]. Then, to show the PSD in dB, it is needed to scale the pressure fluctuations with a reference value $p_{ref} = 2 \cdot 10^5 Pa$ [1].

To better understand the scattering condition, it is also suitable to introduce the cross spectral density matrix (CSD), which is a measure of the correlation between

(a)

(b)
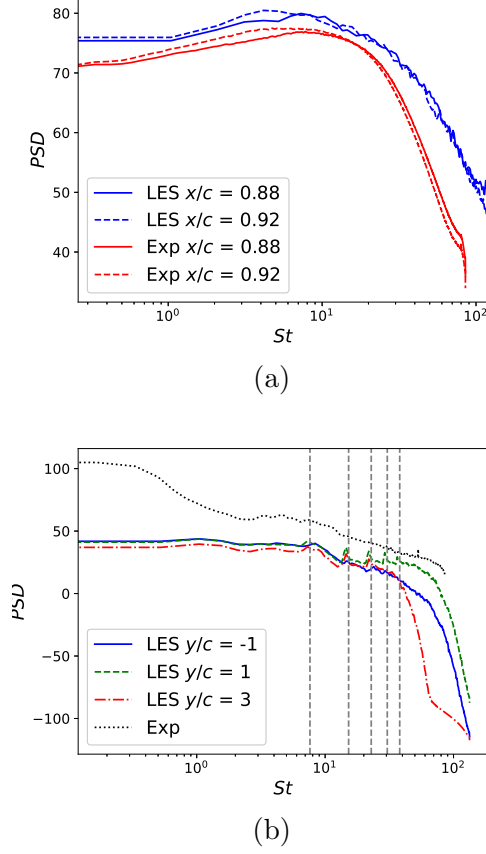
Figure 5.5: PSD of the pressure fluctuations on (a) the suction side at $\frac{x}{c} = 88\%$ and $\frac{x}{c} = 92\%$ and (b) in the acoustic field at $\frac{x}{c} = 1$ and $\frac{y}{c} = [+3, +1, -1]$. The vertical dashed lines in (b) correspond to the scattering condition for the first five wave numbers

signals in the time domain. In our case, the CSD is applied to pressure signals coming from different probes compared to the signal from a single probe located in the acoustic field (positioned as specified in figure 5.6) and is evaluated through the Welch's method, which splits the signal in a finite number of overlapping segments, to whom a window function is then applied. To assess the frequency domain, a Fourier transforming is then used and, for every frequency, the complex value of the signal is averaged over the N segments [8] as:

$$C_{ij} = \frac{1}{N} \sum_{k=1}^{N} p_{i,k}(\omega) p_{j,k}(\omega)^* \qquad (5.1)$$

In figure (5.6), a map of the CSD matrix values for the pressure fluctuations in the acoustic field is reported in the frequency-wavenumber plane. The dashed oblique line represents the scattering wavenumber for each frequency and so, to have propagative waves for a given frequency St we need to look at the part of the map where $k < k(St)$ (hence, left of the dashed line). As it can be seen from the colouring of the CSD values, this is another confirmation that the scattering condition is reached for good part of the studied frequencies, as the highest values of the CSD matrix are located near the k_0 line and to its left.

Finally, the SPOD is performed doing the eigen decomposition of the CSD matrix in order to understand how to decompose and reconstruct the acoustics reducing the complexity of the phenomenon (see appendix B to have a deeper sight of SPOD theory). As it can be seen from figure (5.7)(a), obtained for $He = 15.71$, which is the first discrete Hemoltz number such that $He > He_n$ with $n = 1$, and showing the energy of each SPOD mode, the first three modes, which have approximately the same amplitude and are equally important to describe the physics involved, can reproduce the majority of the farfield pressure. Also, the shape of these modes is reported in figure (5.7)(c), showing sinusoidal-like waves, which can be took into account as Fourier-like modes. Thinking about this, a FFT (fast Fourier trasform) algorithm had been applied to the SPOD modes, obtaining a PSD which is reported in the frequency domain together with the scattering condition for the first wavenumber (vertical dashed line) (fig 5.7)(e), saying once more that the first 3 modes give an exhaustive description of the acoustics, showing also the reaching of the scattering condition and bringing to propagative acoustic waves. Everything that had been said is also consistent with experimental results, shown in figures 5.7(b, d, f), and the small differences can
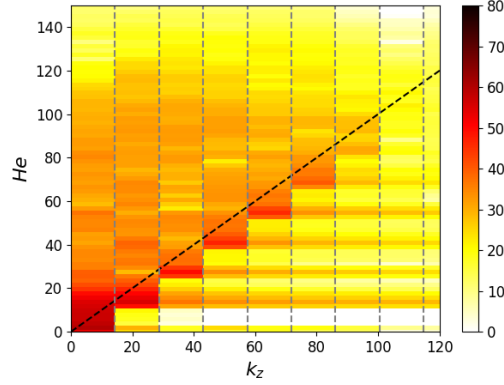
(a)
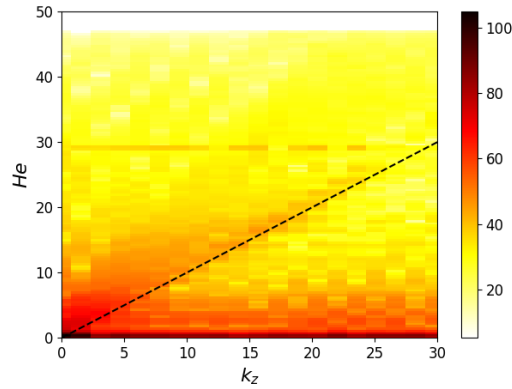
(b)

Figure 5.6: Map of the CSD in a frequency-wavenumber domain. (a) LES: the CSD is performed on the signal obtained from a probe positioned at midspan ($\frac{z}{c} = 21.875\%$), $\frac{x}{c} = 1$, $\frac{y}{c} = 1$. (b) Experimental.

be accounted mainly to the different span length adopted in experiments and simulations. It is also noticeable from figure (5.7)(b) that, for the experiments, also the fourth mode has a high energy, comparable with the first three modes, and could still be considered propagative, even if the PSD coming from its Fourier transforming has a peak for a wavenumber slightly bigger than the scattering one.
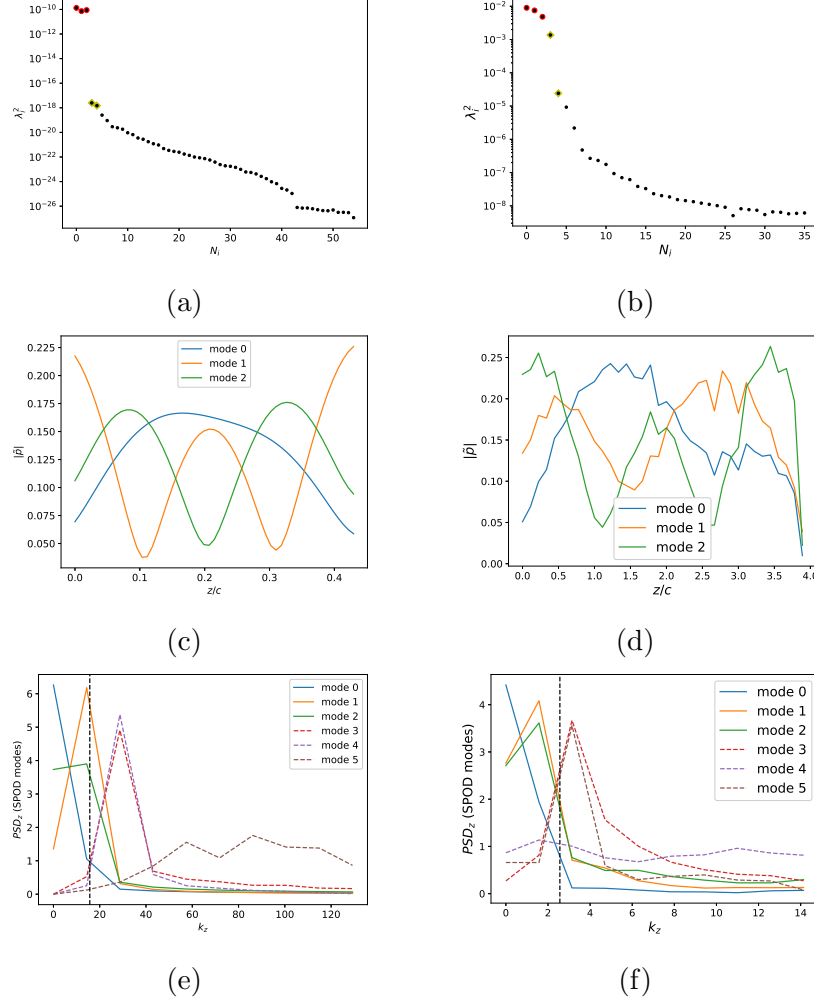
Figure 5.7: (a, b): SPOD modes' energy, showing a clear cut-off between the first three modes and all the other ones. (c, d): SPOD modes' sinusoidal-like shapes. (e, f): PSD of the SPOD modes obtained doing the FFT of the modes themselves. (a, c, e) are from LES, (b, d, f) are from experiments. All these calculations are made at $He = 15.71$ on the acoustic line array located at $\frac{y}{c} = -3$ considering $\frac{3}{4}$ of the span width for the LES, whilst the SPOD is done at $He = 2.56$ for the experimental dataset. Note that two different values of He had been chosen to do this analysis on experimental and numerical datasets, since the span width is different for the two cases and, hence, also the scattering Helmoltz condition changes.

5.1.2.2 Coherence analysis

In this paragraph it will be discussed about the coherence and correlation between sensors on the airfoil surface and in the acoustic field.

To begin, it is useful to introduce the correlation parameter γ, defined as:

$$\gamma_{AB}(\omega) = \frac{\mid C_{AB}(\omega) \mid^2}{P_{AA}(\omega)P_{BB}(\omega)} \tag{5.2}$$

With $0 < \gamma_{AB} < 1$; $C_{AB}(\omega)$ is the CSD matrix of signals A and B, while $P_{AA}(\omega)$, $P_{BB}(\omega)$ are the PSD of signals A and B respectively.

γ (here defined as γ_z, as the spanwise direction is the one considered) will be reported in figure (5.8)(a) to show the correlation between the central sensor in the surface line array at $\frac{x}{c} = 88\%$ and every other sensor in the same line array; this is done to better understand the presence of coherent structures in the spanwise direction, which are likely to induce trailing edge noise. As expected, the maximum coherence is found on the nearest sensors to the reference one, and it reaches a value of $\gamma \approx 0.6$. In figure (5.8)(b) it is reported the same graph but obtained from experimental results, showing that the general behaviour is the same, but the coherence is lower, as the imposition of periodic boundary conditions doesn't exist and also less probes are used on the physical model with respect to the numerical one.

In figure (5.8)(c), also the integral coherence length is reported; it is evaluated as:

$$L_z = \int_0^\infty \gamma_z(\omega, \Delta z)dz \tag{5.3}$$

For both experiments and LES, a coherence length of $L_z = 10^{-2}$ can be found. Dimensionally, if the chord is in millimiters, it would correspond to $L_z = 1mm$, so $\frac{L_z}{c} = 1\%$. Pay attention: the L_z here introduced as coherence length is only a

(a) (b)

(c)
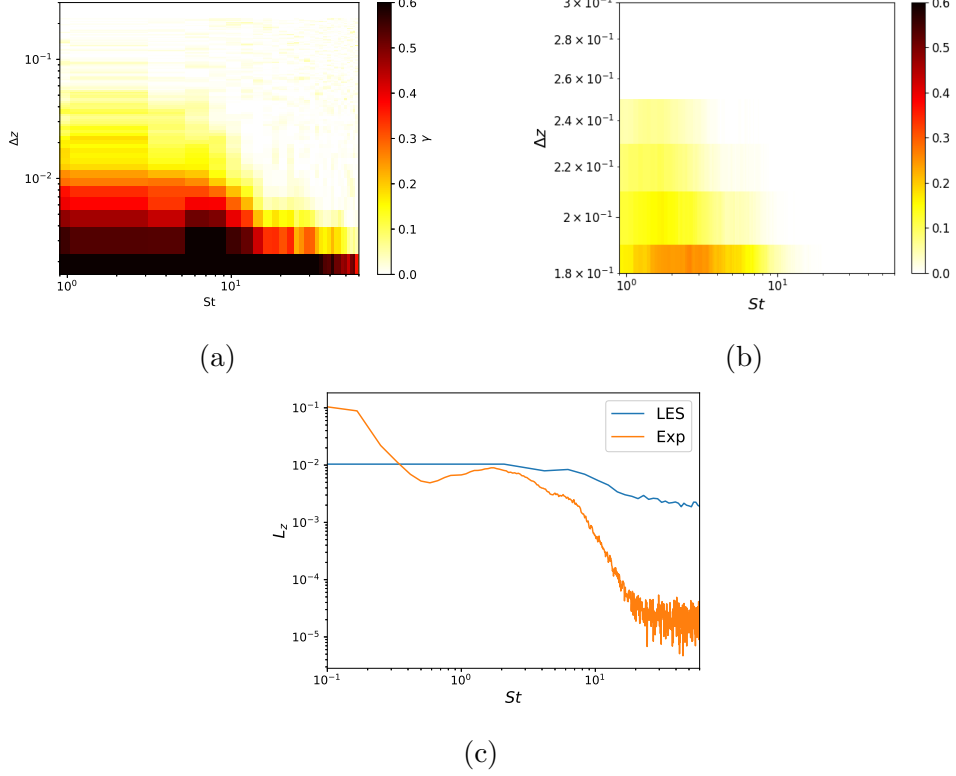
Figure 5.8: (a): Map reporting the coherence between the central sensor in the line array at $\frac{x}{c} = 88\%$ and every other sensor in the same line array (LES). (b) coherence for experiments; considering simmetry, only half of the span width is reported. (c): Integrated coherence length.

measure of coherence along z-direction and has nothing to deal with the spanwise extension of the wing, also referred in this thesis as L_z.

Additionally, to study how the acoustics are affected by fluctuations in the surface pressure and how trailing edge noise is generated, it can be interesting to report the coherence between span-averaged surface line array sensors and the acoustic line array sensors, but to do this, we need to estimate the time shift between the surface pressure fluctuations captured at $\frac{x}{c} = 92\%$ and the acoustic waves captured at $\frac{x}{c} = 1$ and $\frac{y}{c} = 1$. According to the theory [8], the trailing edge noise can be generated in two different ways:

- Back scattering: acoustic waves are generated at the trailing edge and they travel towards surface and acoustic sensors simultaneously. If this is the case, the time shift between the pressure fluctuations at $\frac{x}{c} = 92\%$ and the acoustic waves captured at $\frac{x}{c} = 1$ and $\frac{y}{c} = 1$ will be given by

$$\Delta t = \Delta t_{TE-Acoustics} - \Delta t_{TE-MEMS_{92\%}} \qquad (5.4)$$

With $\Delta t_{TE-Acoustics}$ indicating the time that the acoustic waves spend to go from the trailing edge to the acoustic line array sensors and $\Delta t_{TE-MEMS_{92\%}}$ indicating the same quantity but from trailing edge to surface line array sensors at $\frac{x}{c} = 92\%$.

- Hydrodynamics convection and acoustic propagation: the coherent structures being present in the boundary layer are transported by convection to the trailing edge, where they generate acoustic waves that travel towards the acoustic sensors. In this second case, the time shift would be:

$$\Delta t = \Delta t_{MEMS_{92\%}^{hydro}} + \Delta t_{TE-Acoustics} \qquad (5.5)$$

With $\Delta t_{MEMS_{92\%}^{hydro}}$ being the convective time spent by the turbulent fluctuation to cover the distance between $\frac{x}{c} = 92\%$ and the TE.

The behaviour reported in figure (5.9), depicting the phase shift between surface pressure fluctuations and acoustics, shows that, for the frequencies of interest (where the span averaged mode is dominant), the path with hydrodynamics convection and acoustic propagation is followed. The phase is calculated as a function of frequency following this relation:

$$\phi = \frac{2\pi f \Delta x}{c_{ph}}$$

(a)

(b)
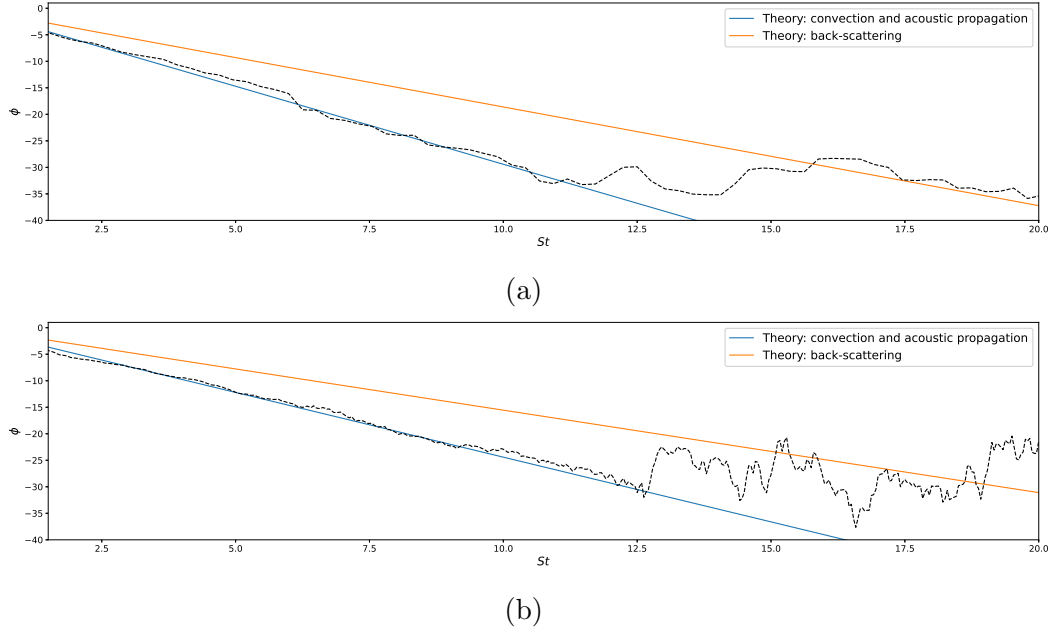
Figure 5.9: Phase shift between surface pressure fluctuations and acoustics. (a) LES. (b) Experimental.
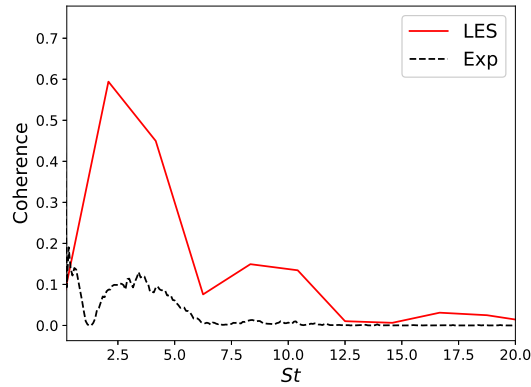
Figure 5.10: Coherence between averaged signals from surface line array at $\frac{x}{c} = 92\%$ and acoustic line array at $\frac{y}{c} = 1$

with c_{ph} being the phase velocity, evaluated experimentally in [1] as $c_{ph} = 0.6U_\infty$ for the hydrodynamics, whilst it is equivalent to the sound velocity for the acoustics. Also experimental data follow this behaviour, visible at figure (5.9)(b). Then, the time delay evaluated as in (5.5) is considered to study the coherence

between span-averaged surface sensors and acoustic sensors, which is showed in figure (5.10), both for numerical and experimental data.

5.2 Case with free stream turbulence $(Tu = 1\%)$

In this section everything that had been introduced in section (5.1) for the simulation without free stream turbulence, will be reported for the simulation with FST; If the results are similar, no further investigation will be brought, whereas we will focus on the results that differ the most.

5.2.1 Flow field

Here it will be reported about the hydrodynamics results coming from the large eddy simulation done with free stream turbulence $(Tu = 1\%)$. The analysis carried on the acoustic field coming from the same simulation will be detailed in section 5.2.2.

In figure 5.11, we show a snapshot of the flow field where the Q-criterion colored with magnitude of the streamwise velocity is presented.
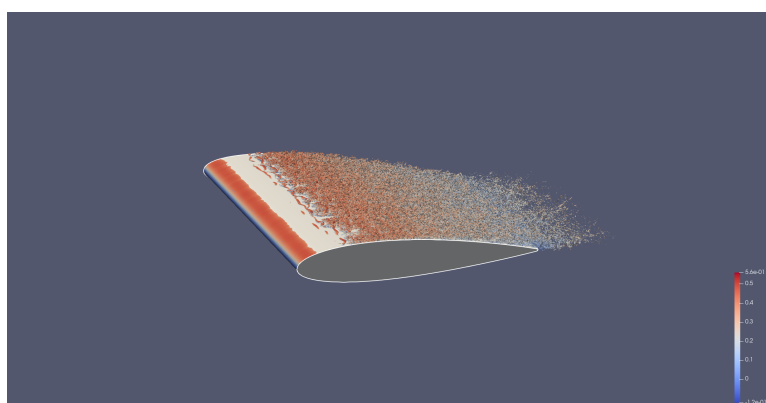
Figure 5.11: Q-criterion of the FST simulation, coloured by streamwise velocity.

5.2.1.1 Wall quantities and boundary layer velocity profiles
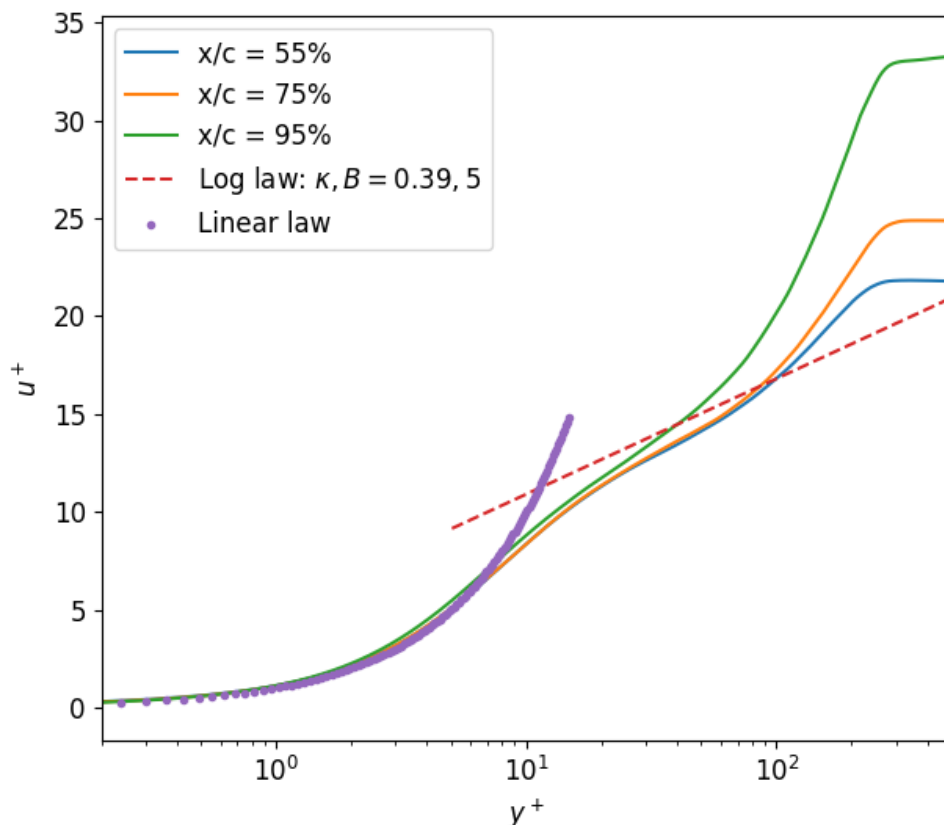
Figure 5.12: Law of the wall.

As visible from figure (5.12), as far as the u^+ trend with respect to y^+ is concerned, almost nothing changed from figure (5.1), testifying the goodness of the results coming from both LESs.

Speaking about the boundary layer velocity profiles, some differences are noticeable from the case without FST shown in figure (5.2). Contrary to what would be natural to think, the velocity profiles look shifted up-left, as if the flow was more separated than in the case without FST. Looking deeply into it, this is consistent with the C_f behaviour: at each of the considered measuring stations,
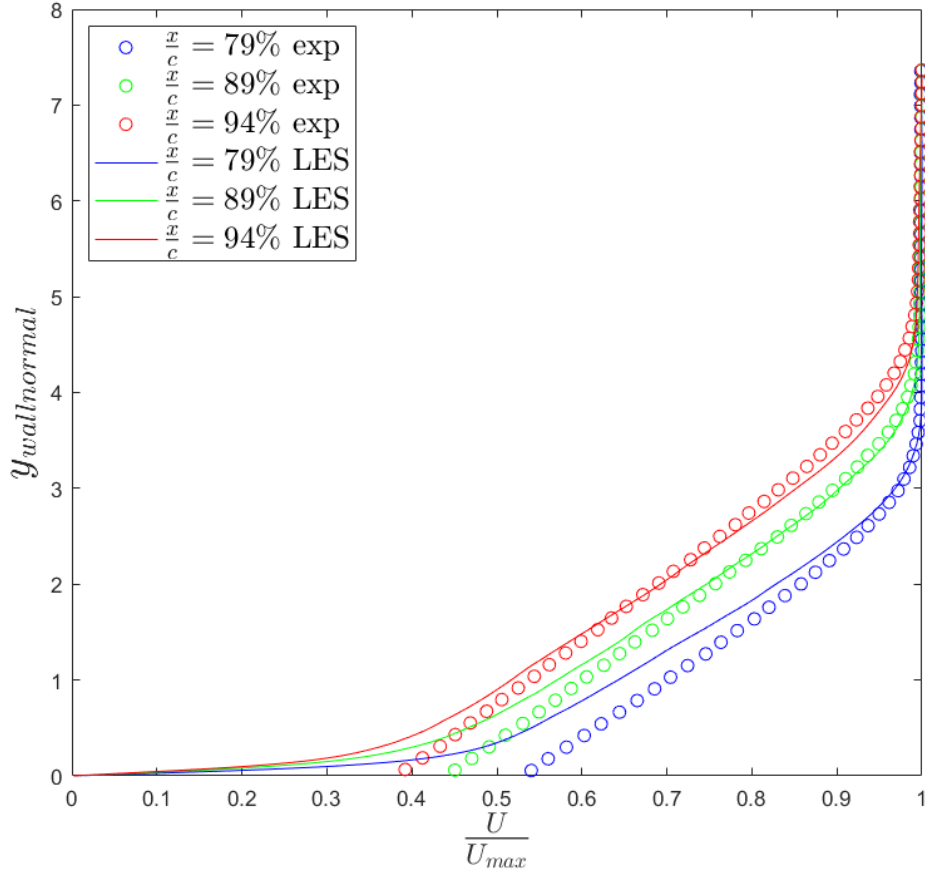
Figure 5.13: Boundary layer normalized velocity profiles.

the C_f value is higher for the case without FST than for the case with FST and this means that the boundary layer is actually less turbulent for the case with FST injection. This is understandable thinking that, injecting a certain level of FST in the base flow, the transition changes and, in particular, the laminar separation bubble located near the LE, is shorter and thinner and this results in a more gradual reattachment of the flow, which can make it more stable and consequently, less turbulent downstream the reattachment point. And, in agreement with this, the C_f after the reattachment point is smaller than for the case without turbulent injection.

Speaking quantitatively, the main differences are outlined in table (5.1) for the station located at $\frac{x}{c} = 94\%$.

	τ_w	C_f
$Tu = 0\%$	$1.54 \cdot 10^{-4}$	0.0035
$Tu = 1\%$	$1.48 \cdot 10^{-4}$	0.0033

Table 5.1: Differences in the turbulent boundary layer at $\frac{x}{c} = 94\%$ for the two simulations (with and without FST).

Note that there is a direct proportionality between τ_{wall} and u_τ and this brings also the plateau of u^+ to be at higher u^+ values for the simulation with FST than for the one without it.

5.2.1.2 C_p

As it has been underlined in paragraph 5.1.1.2, it had been needed to set a simulation with free stream turbulence ($Tu = 1\%$) in order to be more realistic on the position of the recirculation bubble which causes a drop in the C_p distribution over the suction side of the airfoil.

Here, we will show the results from this simulation.

As it can be deduced looking at figure (5.14), the location of the bubble and its starting point are this time better captured. It is visible also that the C_p drop for the LES is smoother than for experiments, and this may be accounted for the different Mach and a different level of FST: due to the non-homogeneity of the free stream turbulence in the experimental data indeed, it hadn't been possible to impose the exact same amount of FST in the numerical simulation; however, after some tests with different levels of Tu and turbulence length scale, performed over a limited amount of CTUs, the C_p distribution obtained with $Tu = 1\%$ in the free stream had been considered sufficiently good and this value of turbulence intensity had been imposed for the rest of the simulation.
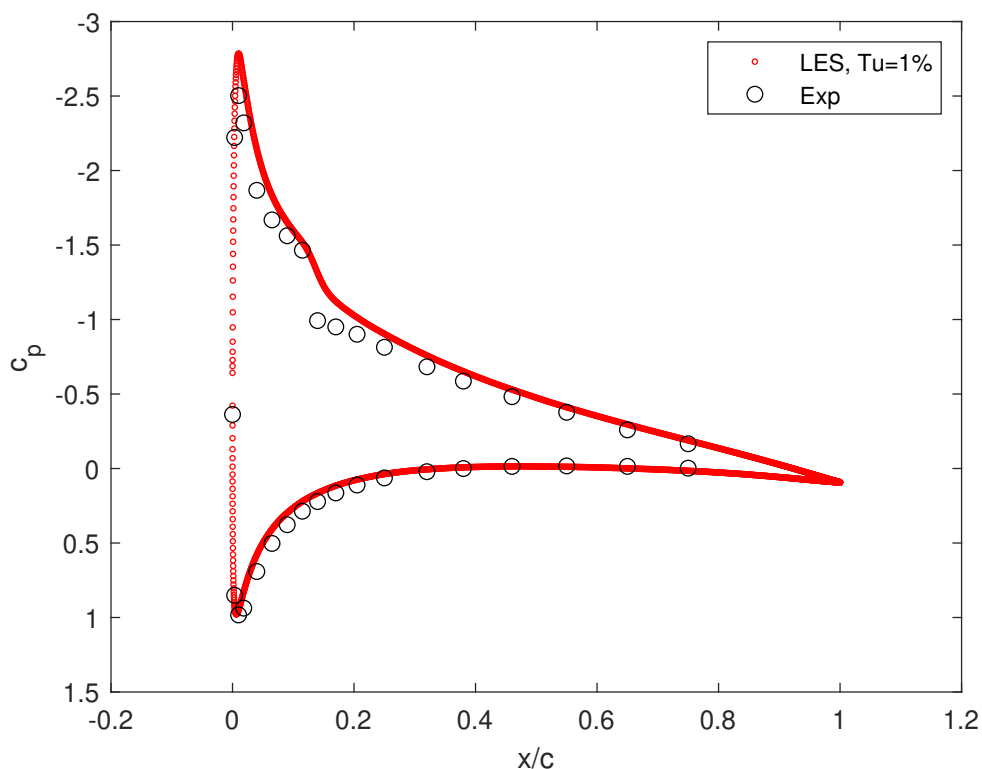
Figure 5.14: Pressure coefficient distribution coming from experimental campaign (black dots) and LES with FST $(Tu = 1\%)$ (red dots). Pay attention to the sign of C_p in the y-axis: the graph had been inverted to show the C_p from suction side on the upper part and the one from pressure side on the lower part of the plot.

5.2.1.3 C_f

As far as the C_f distribution for the simulation with $Tu = 1\%$ is concerned, it is interesting to underline some differences registered with respect to the C_f distribution visible at figure (5.4), coming from the simulation without free stream turbulence. As expected, the FST had delayed the appearing of the laminar separation bubble: comparing to the case without FST, where the starting point was located at $\frac{x}{c} = 4.7\%$, this time the bubble starts at $\frac{x}{c} = 7.5\%$. Also the reattachment point has moved, changing location from $\frac{x}{c} = 18.4\%$ to $\frac{x}{c} = 12.5\%$, making the bubble shorter.
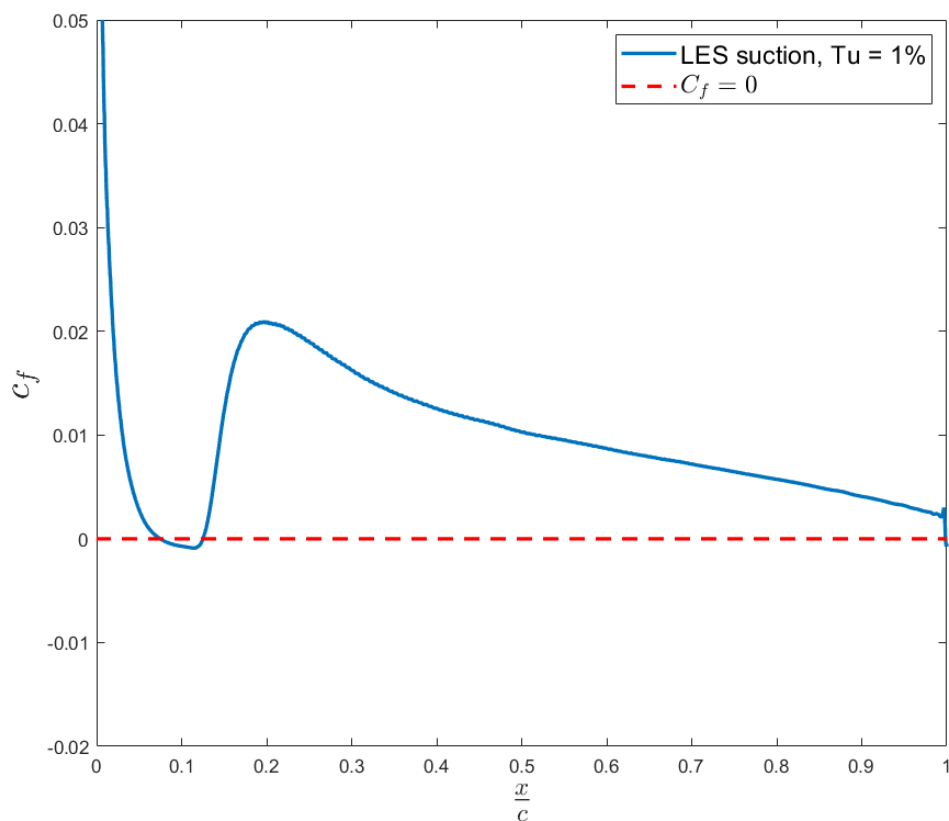
Figure 5.15: Skin friction coefficient for the LES with free stream turbulence; results from 1500 span-averaged snapshots, covering 22.5 CTUs

Finally, it is interesting to show that, as a certain amount of turbulence is already present in the base flow, the bubble becomes thinner and this results in a smaller C_f drop: we moved from $min(C_f) = -0.0074$ to $min(C_f) = -0.0009$, and the transition point is now difficult to decipher. However, the FST has certainly anticipated the transition to turbulence.

5.2.2   Acoustic field

As far as the acoustics are concerned, all results are almost identical, so the same plots that had been reported in section (5.1.2) will be reported again, this time

for the simulation with FST, versus the experimental results.

5.2.2.1 Scattering condition

(a)

(b)
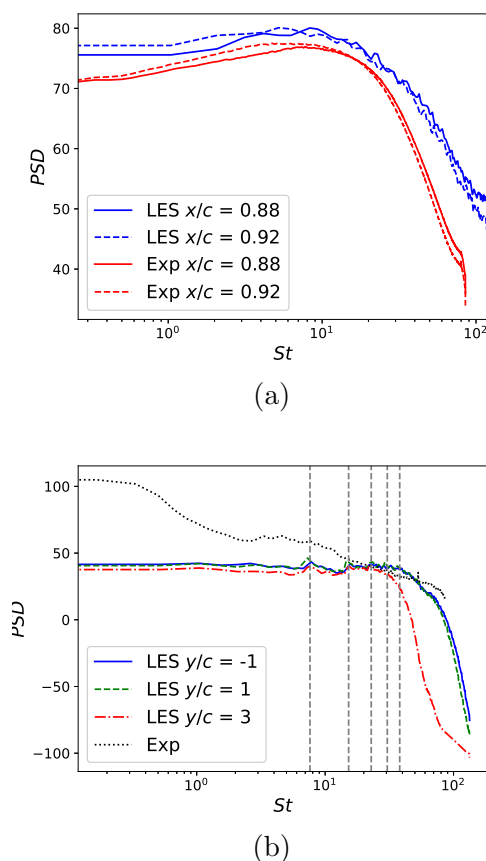
Figure 5.16: PSD of the pressure fluctuations on (a) the suction side at $\frac{x}{c} = 88\%$ and $\frac{x}{c} = 92\%$ and (b) in the acoustic field at $\frac{x}{c} = 1$ and $\frac{y}{c} = [+3, +1, -1]$. The vertical dashed lines in (b) correspond to the scattering condition for the first five wave numbers

Looking at figure (5.16), almost identical to figure (5.5) obtained for the case without FST, it can be seen how close are the PSD values coming from the surface line arrays at $\frac{x}{c} = 88\%$ and $\frac{x}{c} = 92\%$. Moreover, focusing on the spectra coming from the acoustic line array, the agreement with experimental data is slightly

better then the one visible in figure (5.5).
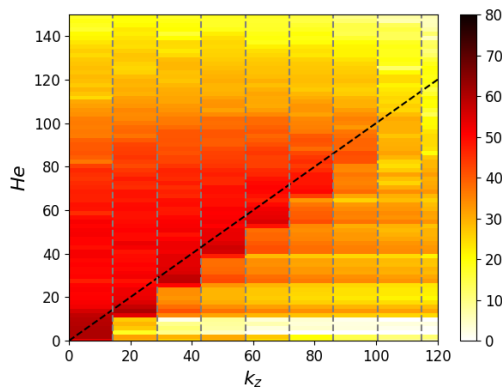
(a)
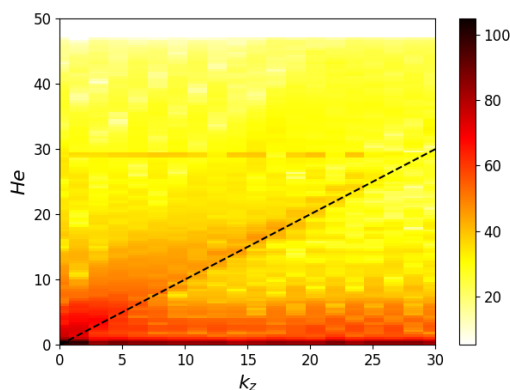
(b)

Figure 5.17: Map of the CSD in a frequency-wavenumber domain. (a) LES: the CSD is performed on the signal obtained from a probe positioned at midspan ($\frac{z}{c} = 21.875\%$), $\frac{x}{c} = 1$, $\frac{y}{c} = 1$. (b) Experimental.

Looking at figure (5.17), everything that had been said for the simulation without FST is still valid; the only noticeable difference with figure (5.6) is that, looking at the CSD map, the overall value is a little bit higher and, considering that the CSD comes from the squared values of the pressure fluctuations, a flow which contains a higher degree of turbulence can lead to a higher CSD.

As far as the SPOD is concerned, the exact same behaviour noticed in the no-FST simulation (figure (5.7)) is also visible from figure (5.18), where a huge
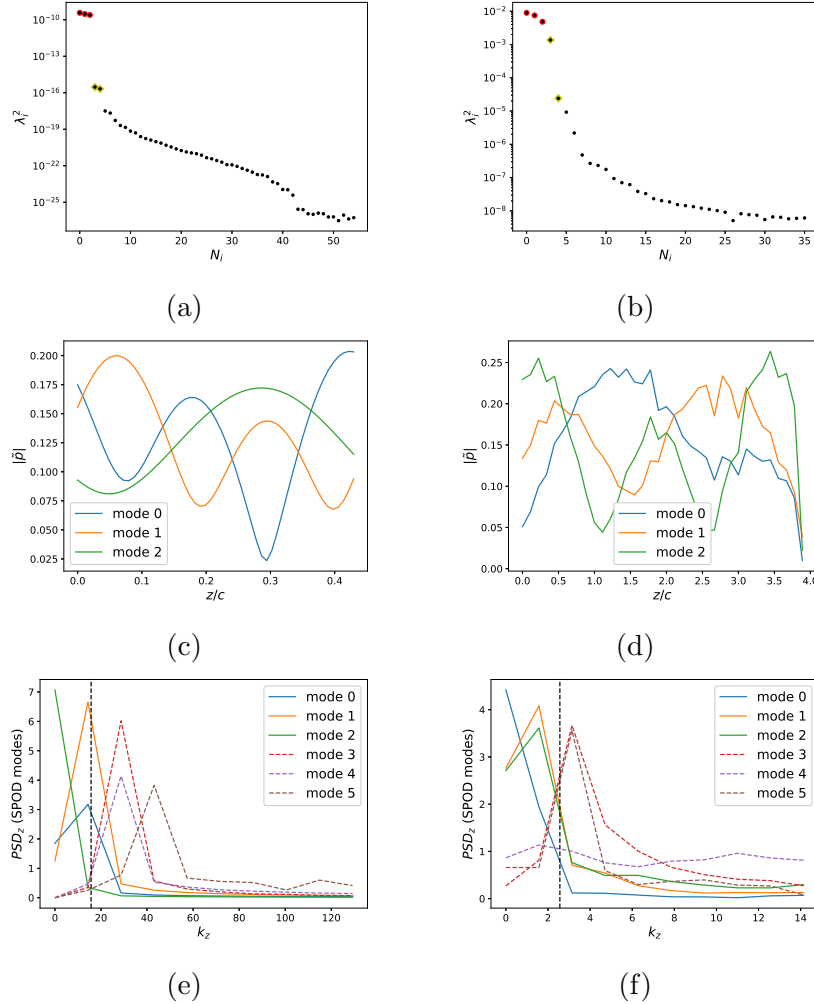
Figure 5.18: (a, b): SPOD modes' energy, showing a clear cut-off between the first three modes and all the other ones. (c, d): SPOD modes' sinusoidal-like shapes. (e, f): PSD of the SPOD modes obtained doing the FFT of the modes themselves. (a, c, e) are from LES, (b, d, f) are from experiments. All these calculations are made at $He = 15.71$ on the acoustic line array located at $\frac{y}{c} = -3$ considering $\frac{3}{4}$ of the span width for the LES, whilst the SPOD is done at $He = 2.56$ for the experimental dataset. Note that two different values of He had been chosen to do this analysis on experimental and numerical dataset, since the span width is different for the two cases and, hence, also the scattering Helmoltz condition changes.

drop shows itself after the first three modes. Also the modes' shape is similar to the simulation without free stream turbulence, with the only difference of the

spacial phase alongside the span direction. Applying the FFT in span, the results are consequently very similar.

5.2.2.2 Coherence analysis

(a)

(b)

(c)
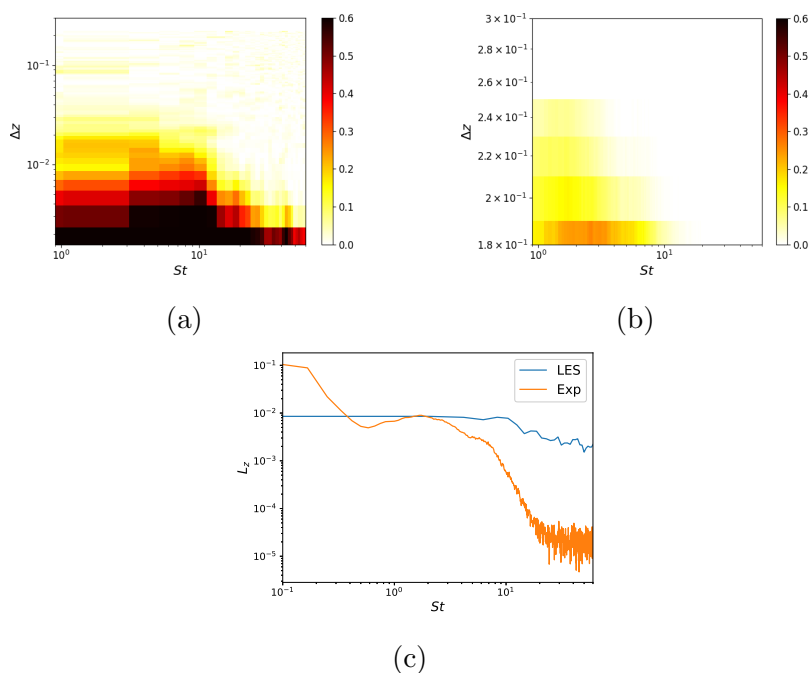
Figure 5.19: (a): Map reporting the coherence between the central sensor in the line array at $\frac{x}{c} = 88\%$ and every other sensor of the same array (LES). (b) coherence for experiments; considering simmetry, only one side is reported. (c): Integrated coherence length.

Also the results coming from the coherence analysis are overlapping the ones obtained without free stream turbulence. An interesting thing, noticeable both in figures (5.8) and (5.19) is that an higher coherence is present near $St = 10$, and, remarkably, this is the same value where we have the hump on the MEMs PSD spectra.

Finally, from figure (5.20)(a) it is visible that the first wavenumber is dominant until $St \approx 9$, whereas for the LES without FST (5.9)(a)) it was dominant until

(a)

(b)
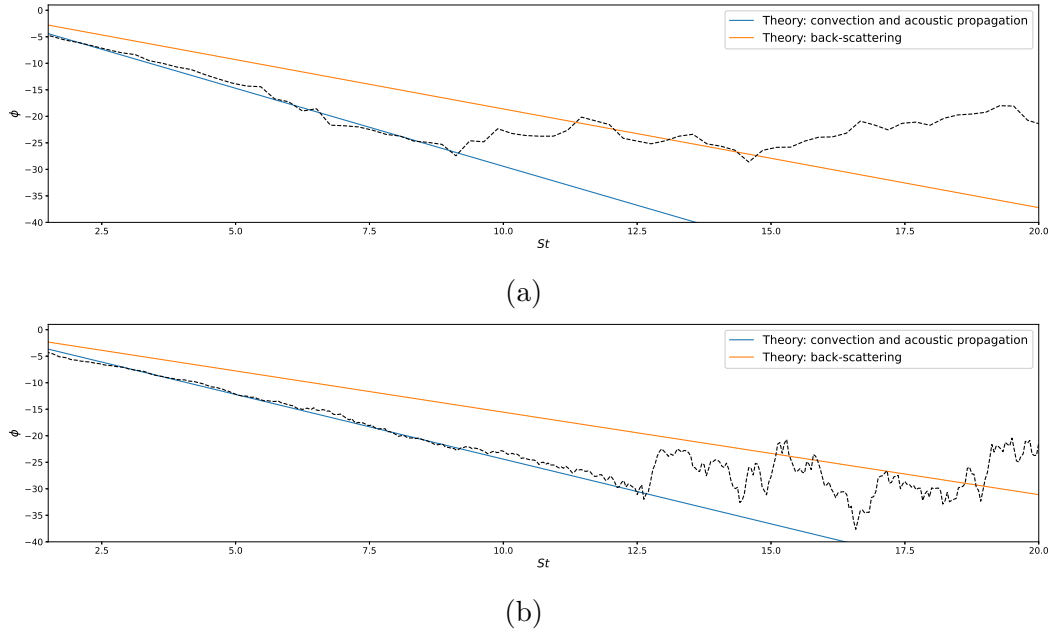
Figure 5.20: Phase shift between surface pressure fluctuations and acoustics. (a) LES. (b) Experimental.

Figure 5.21: Coherence between averaged signals from surface line array at $\frac{x}{c} = 92\%$ and acoustic line array at $\frac{y}{c} = 1$

$St \approx 11$. The coherence between SPF (surface pressure fluctuations) and acoustic waves visible in figure (5.21) is almost identical to the one at figure (5.10).

5.2.3   SPOD of the whole acoustic field

This paragraph will be accounted for the spectral proper orthogonal decomposition (SPOD) of the whole acoustic field (see the appendix B to have a better understanding of SPOD's theory and implementation).
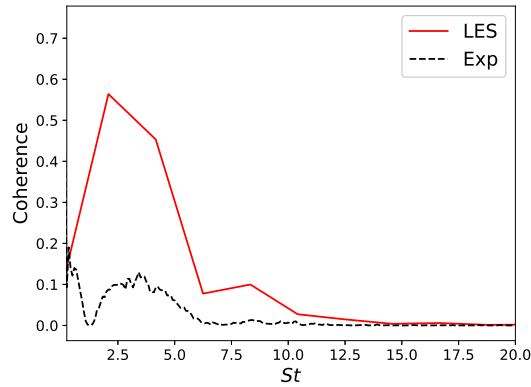
Considering that, regarding the acoustic field, both simulations brought to similar results, slightly better for the simulation with FST (in particular, the acoustic spectra shown in figure (5.16)(b) have a very good agreement with experimental data), the SPOD had been performed only on the dataset coming from this simulation, exception made for a quick comparison that will be shown to compare also a mode shape coming from the simulation without FST injection.

Prior to the SPOD itself, an interpolation on the farfield mesh had been necessary, since we want to look at acoustic waves that spread from the trailing edge of the wing towards the surroundings and considering that far from the airfoil the mesh gets coarse. On the near wall region, constituted by hexaedral elements, a spanwise Fourier transform of the solution had been performed to extract Fourier modes: these had been used later to compute the SPOD of the pressure and hydrodynamic field.

5.2.3.1   Pressure SPOD

Here we will show the SPOD coming from the pressure field, hence substituting $\hat{q}$ with $\hat{p}$ in (B.3). Initially, the SPOD had been performed on a pressure signal covering 28.15 CTUs sampled at 0.2 Hz. However, some non-physical behaviours had been noticed; indeed, plotting the first SPOD mode's shape at the energy peak's frequency, it is possible to see very small structures on its suction side (figure (5.22)(b, c)).

These small structures were believed to come from aliasing effect, since the sampling frequency had been quite low, so that high frequencies in the SPOD

(a)

(b)

(c)
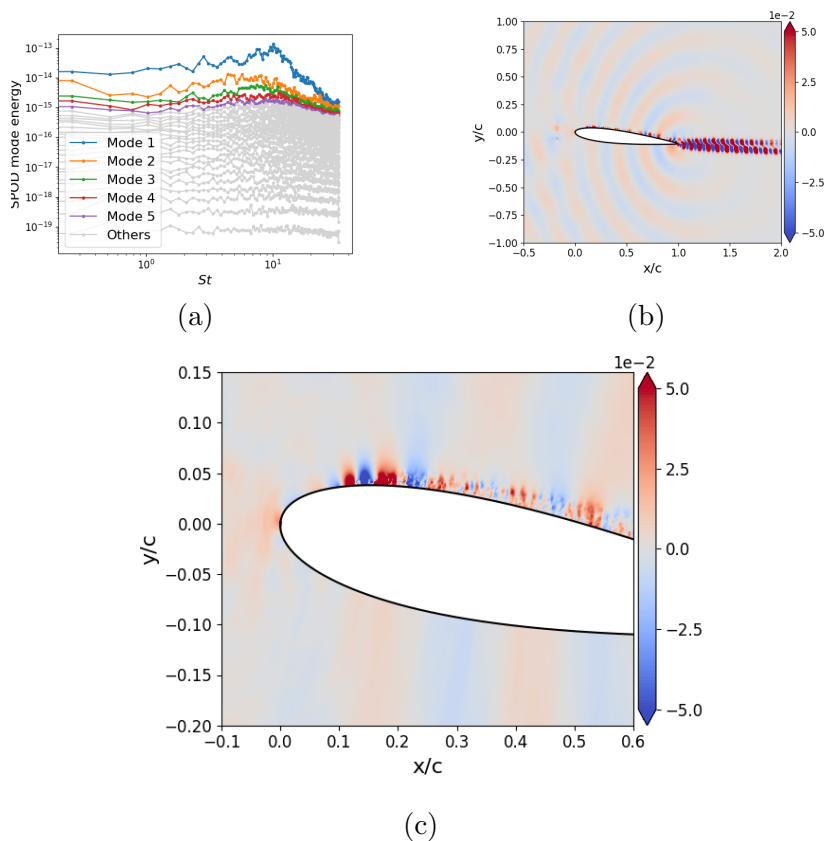
Figure 5.22: (a) SPOD modes' energy spectrum, coming from the first spanwise FFt mode (k_z^0); (b) Shape of the first SPOD mode at $St = 9.38$; (c) Zoom-up of (b). a, b and c come from the dataset sampled at 0.2 Hz

field could have been aliased to low frequencies. Taking this into account, it had been considered useful to run a shorter simulation at an higher sampling rate, so that the aliasing problem could vanish, even if performing the SPOD on a shorter time signal is of course less accurate in the results.

All the results shown below, from figure (5.23) onwards, are obtained over 5 CTUs of simulation with sampling frequency of 0.8 Hz.

In figure (5.23), it is reported the energy spectrum of the SPOD modes computed on the first Fourier mode (so isolating the k_z^0 wavenumber). It is easy to see how all the modes have a similar spectrum but characterized by different en-

Figure 5.23: SPOD's modes energy spectrum. Sampling frequency 0.8 Hz

ergies: the first mode is almost one order of magnitude greater than the second one. As the energy decreases exponentially going through the modes, a deeper analysis will be reported only on the first two ones.

Looking at figure (5.24), the evolution of the first mode's shape is reported at increasing frequencies on the left column, considering the main peaks visible in the energy spectrum; the same is done on the right column for the second mode.
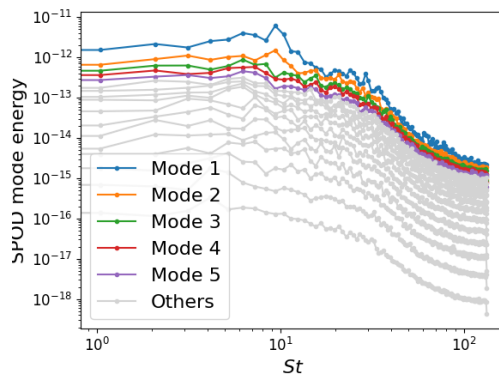
As it was already visible from the energy spectrum, the modes have similar shapes and follow a similar behaviour. What's interesting to see is that, increasing the frequency, the main acoustic source moves from the trailing edge, upstream to $\frac{x}{c} = -0.18$ and this was not expected a priori. On that location indeed, as reported in section 4, a level of free stream turbulence is injected in the field and it behaves as a noise source that gets more and more dominant as the frequency increases. At $St = 9.38$ (figure (5.24) (c,d)) both sources seem to have similar intensities and interact creating evanescent reflection zones. This behaviour is obviously non-physical, but since it characterizes high frequencies and is more present on low-energetic modes, the general behaviour is still acceptable.

Focusing on the best results, it is interesting also to see that the laminar separation bubble has an influence on the mode shape: looking at the first SPOD
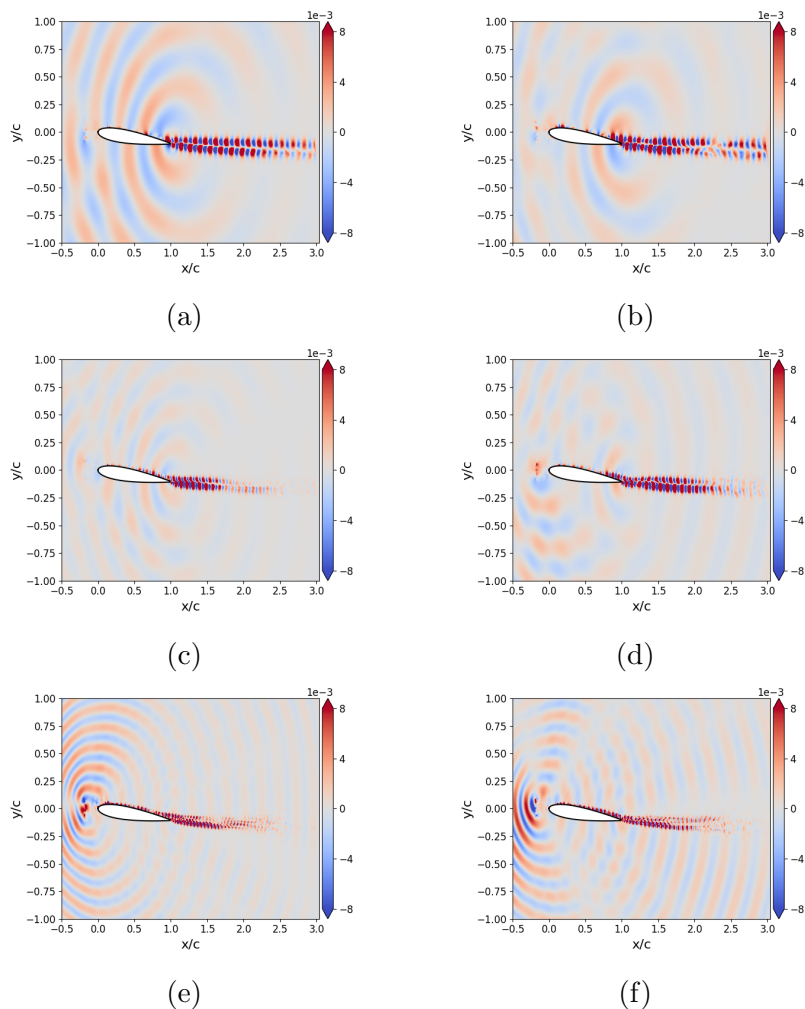
Figure 5.24: (a, c, e) mode shapes for the first SPOD mode at $St = 6.25$, $St = 9.38$ and $St = 18.75$ respectively. (b, d, f) mode shapes for the second SPOD mode at $St = 6.25$, $St = 9.38$ and $St = 15.62$ respectively.

mode and zooming up to the profile (see figure (5.25)), a different pattern is clearly noticeable starting from the recirculation zone examined studying the C_p and C_f distributions. Very tiny structures are visible arising from the bubble zone, and this could still be an aliasing effect, but much less evident than the one highlighted in figure (5.22)(c).

As it could be seen from appendix B, the SPOD is done passing the elemets'
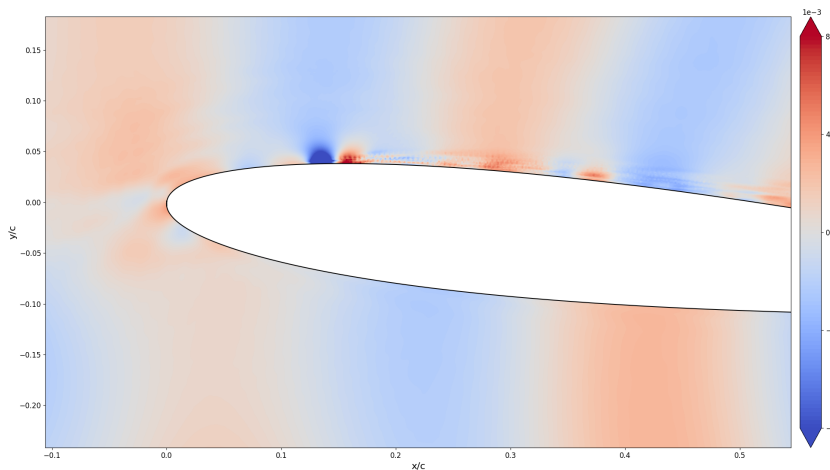
Figure 5.25: Zoom-up on the first SPOD mode's shape at $St = 6.25$

(a)	(b)
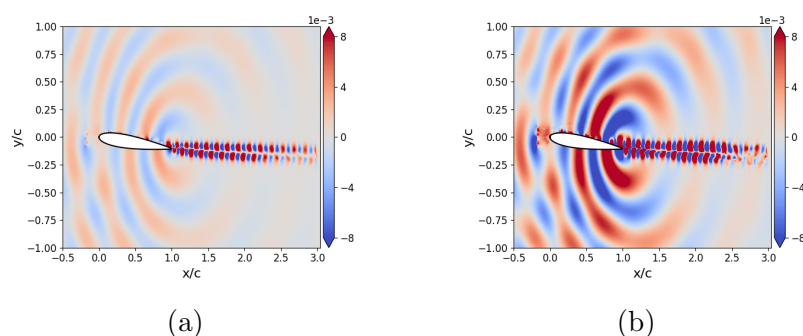
Figure 5.26: (a) mode shape for the first mode at $St = 6.25$ using the same weights on the whole acoustic field. (b) mode shape for the first mode at $St = 6.25$ restricting the weighting zone to the close-trailing edge area.

areas to the weights W. All the results above reported had been obtained computing the weights in the same way on the whole field. To see how the noise spreads from the trailing edge, it can be interesting also to restrict the weighting zone to a limited area close to the trailing edge of the wing. Doing so, the acoustic waves spreding from there are even more evident, as it can be seen from figure (5.26).

Another analysis had been carried on the SPOD coming from the first spanwise
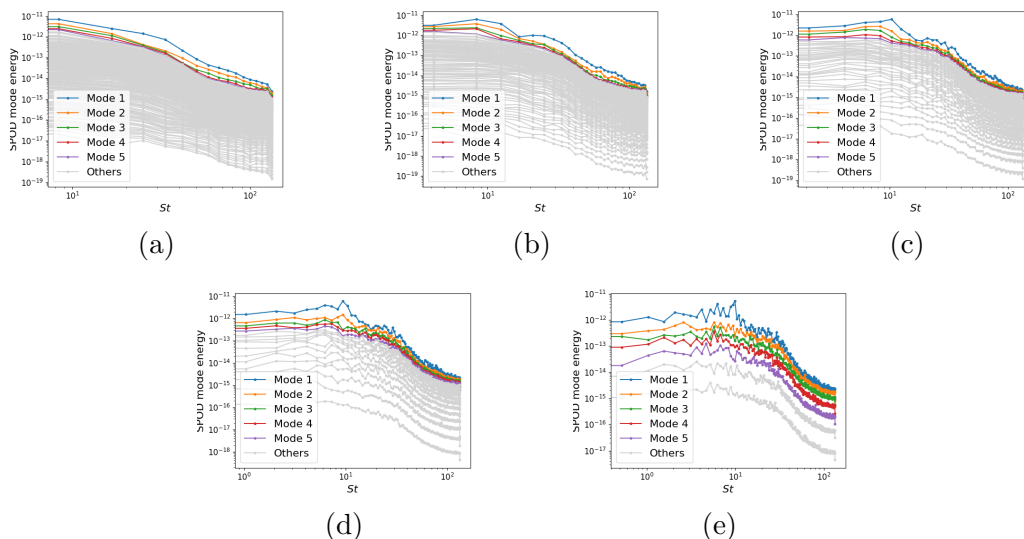
Figure 5.27: SPOD modes' energy obtained using a different number of discrete Fourier transformed modes. (a) $ndft = 32$, (b) $ndft = 64$, (c) $ndft = 128$, (d) $ndft = 256$, (e) $ndft = 512$. The SPOD had been performed weighting with the elemets' area over the whole domain.
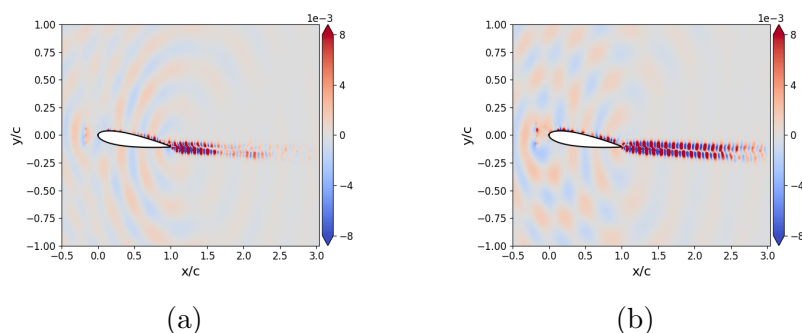
Figure 5.28: First SPOD mode's shape at $St = 8.33$ with (a) ndft = 32 and (b) ndft = 512.

Fourier mode, to see which influence the number of discrete Fourier transformed modes has on the resolution of the SPOD modes themselves. Looking at figure (5.27), it is possible to see how all the spectra obviously follow the same descending trend, though with an increasing number of discrete points, passing from $ndft = 32$ to $ndft = 512$. The highest this number, the highest the resolution on

the modes' shape (also, the highest the noise). However, this does not affect too much the modes' shape, as visible from figure (5.28), which compares the first SPOD mode's shape extracted at the same $St = 8.33$ with ndft = 32 and ndft = 512, even if with ndft = 32 the wavepackages are not converged. Considering this aspect, as the resolution of the modes' shape with $ndft = 256$ had been considered sufficiently good within the range of frequencies $St < 10$, henceforth all the displayed results have been obtained with that setting.

Another interesting analysis can be carried comparing the acoustic field SPOD obtained from different spanwise Fourier modes, starting from the first one, which correspond to the $0th$ spanwise wavenumber. In figure (5.29), it is possible to see the SPOD mode's shapes coming from the first FFT mode (k_z^0) (figs (a) and (b)), from the second FFT mode (k_z^1) (figs (c) and (d)), from the third FFT mode (k_z^2) (figs (e) and (f)) and from the fourth FFT mode (k_z^3) (figs (g) and (h)). On the left column we have the results for $St = 6.25$, whilst on the right one there are the results obtained with $St = 9.38$. It is interesting to see how the scattering condition is achieved considering different spanwise wavenumbers: as specified in section 2.2.2, to have propagative acoustic waves shedding from the trailing edge of the profile, it is needed to have $St > St_n$, where n represents the n-index of the considered spanwise wavenumber. For n=0, the scattering condition is always achieved and, indeed, it is possible to see TE noise at $St = 6.25$ as well as at $St = 9.38$. Moving to n=1, to have trailing edge noise it is necessary to meet the condition $St > St_1 = \frac{1c}{L_z M} = 7.62$ and, as expected, the TE noise is much more visible for $St = 9.38$ than for $St = 6.25$. For $n = 2$ and $n = 3$ the scattering condition would be fixed at $St > 15.24$ and $St > 22.86$ respectively and this is, for both cases, higher than $St = 6.25$ and $St = 9.38$, resulting in no sound waves visible at figure (5.29)(e, f, g, h).

Finally, before moving to the SPOD made on the velocity u and v signals, we
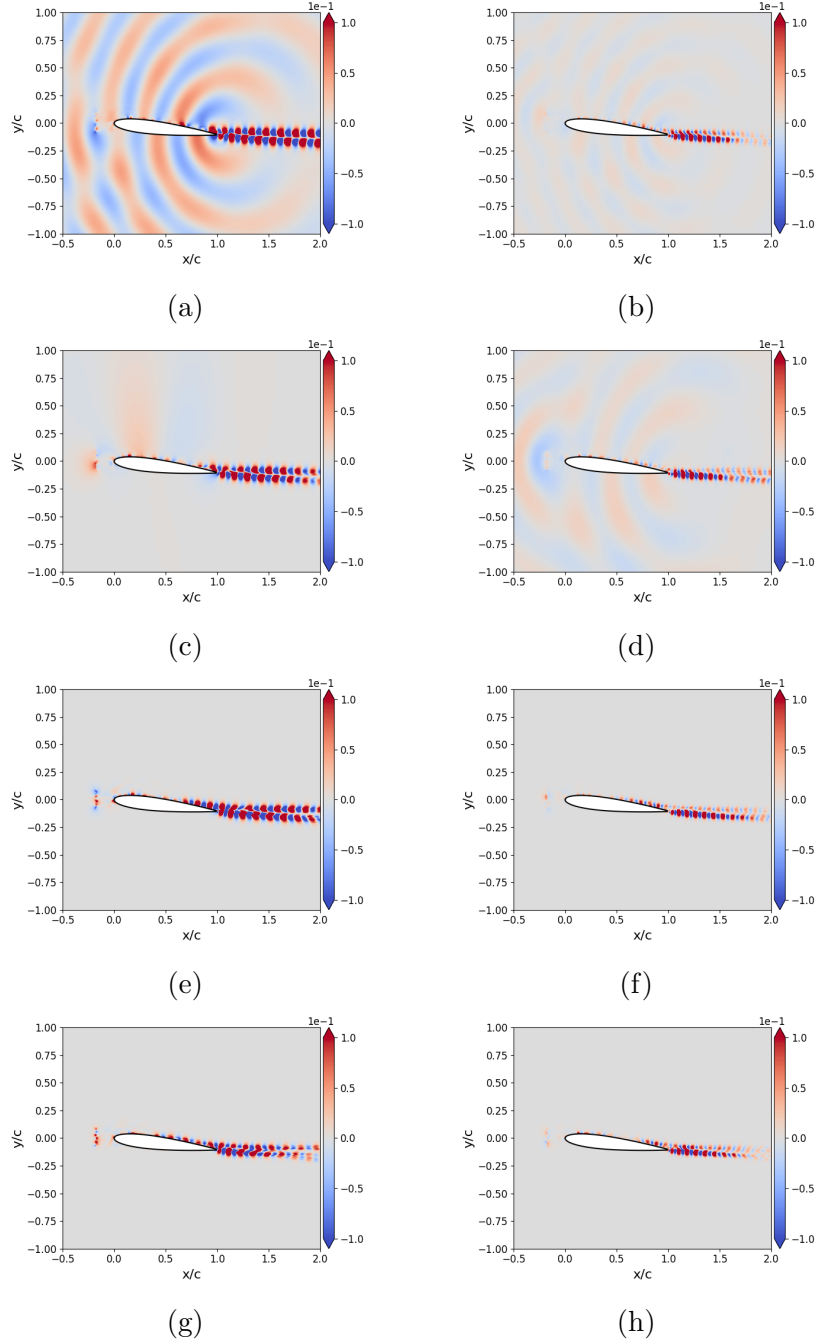
Figure 5.29: SPOD mode's shapes at (a, c, e, g) $St = 6.25$; (b, d, f, h) at $St = 9.38$. (a, b) for k_z^0; (c, d) for k_z^1; (e, f) for k_z^2; (g, h) for k_z^3.

will show in figure (5.30)(a) the energy spectrum, and (b) the first SPOD mode shape at $St = 9.38$, coming from the dataset without FST (sampled at 0.2 Hz, indeed the aliasing problem is visible on the suction side of the airfoil), to show how the acoustic field looks like without the FST injection zone.
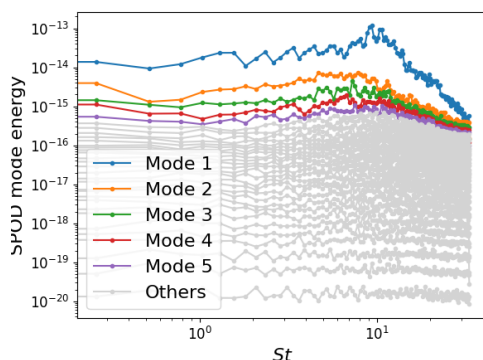
(a)
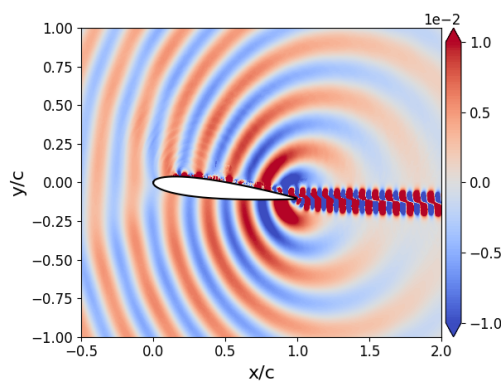
(b)

Figure 5.30: SPOD energy spectrum (a) and SPOD first mode shape at $St = 9.38$(b), for the dataset without FST, sampled at 0.2 Hz.

We report that, different things have been tried to artificially "delete" the FST injection zone which modifies the acoustics for the simulation with FST, but unsuccessfully, since it affects the whole spectrum. In the future, it would be interesting to try different filtering approaches, identifying the main disturbing frequency and dumping it artificially.

5.2.3.2 Hydrodynamic SPOD

Here we will show the SPOD coming from the hydrodynamic field, hence substituting $\hat{q}$ with $\hat{u}$ and $\hat{v}$ in (B.3).

In figure (5.31), the mode shapes coming from the hydrodynamic field are shown. The investigated frequencies are the same chosen for the first pressure SPOD mode analyzed in figure (5.24)(a, c), exclusion made for the highest frequency, which is characterized by really small wavepackages.

(a)

(b)

(c)

(d)

Figure 5.31: (a, c) mode shapes for the first $\hat{u}$ field SPOD mode at $St = 6.25$ and $St = 9.38$ respectively. (b, d) mode shapes for the first $\hat{v}$ field SPOD mode at $St = 6.25$ and $St = 9.38$ respectively.
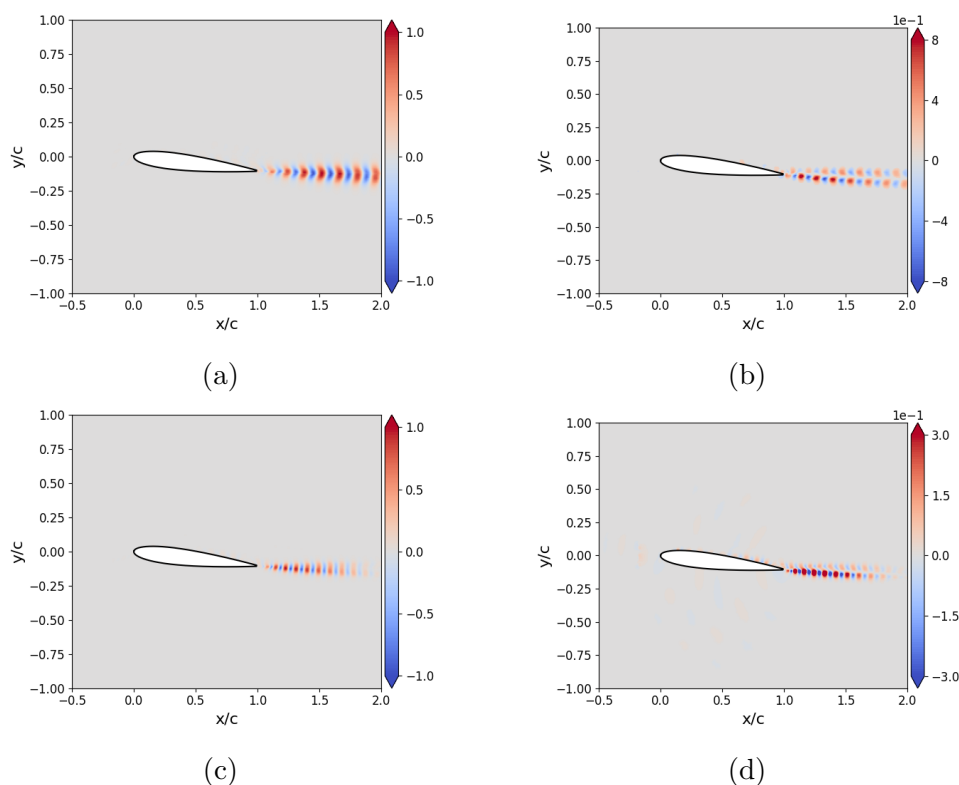
As the focus here is on hydrodynamics and not on acoustics, figures (5.31)(a, b, c, d) have been normalized and adjusted to exclude the fluctuations in the domain consequent to the acoustic waves.

Chapter 6

Conclusions

Here, two large-eddy simulations have been performed on a three dimensional wing extruded from a NACA0012 airfoil, using the open source solver PyFR. The aim of these simulations has been to understand the wave generation mechanism and the resulted acoustic field. The studied geometry and flow conditions correspond to the experiments performed at TU Berlin [1]. We have also studied the effects of free-stream turbulence level on the flow and acoustic fields by considering $Tu = 0$ and 1%.

It was found that the flow over the wing was sensitive to small changes in Tu levels. A large separation was found close to the leading edge for $Tu = 0$. The best agreement between the measured and computed flow filed was observed in the case of $Tu = 1\%$, where the separated area was significantly reduced in size. However, as the turbulence generation forcing is not divergence free, it acted as a noise source.

What can be understood is that there is a strong bond between the scattering condition and wing span width. The presence of coherent structures inside the boundary layer, indeed, has been noted to be the most important noise generation source. This is even more evident looking at the analysis of the SPOD mode shapes for different spanwise wavenumbers (different Fourier modes evaluated in

the span direction).

The large data set generated here, with the main focus on studying the trailing-edge noise generation, can be used in the future studies for further analysis. An example is the resolvent analysis which can identify the dominant structures, which later can be used for noise control.

Appendix A

PyFR Turbulence plugin

As it had been underlined many times in the body of the thesis, this whole work is about showing and explaining the results from two large eddy simulations (LES), implemented with the Flow Reconstruction solver PyFR. A little bit about this tool has already been said in the introduction and in the followings, but this appendix is specific for a deeper explanation of the PyFR turbulence plugin used to inject synthetic turbulence in the base flow for one of the two simulations made. The goal of all the research behind this thesis was not to implement nor to develop any part of the solver itself, so here we will focus only on simply explaining what's been understood to stand as a basis for the simulation itself. The main reference, together with the PyFR online forum where the developers are always ready to dispel doubts, is a paper from Giangaspero G., Witherden F. and Vincent P. [10].

In the field of high order simulations, the injection of synthetic turbulence can be useful for many aspects: one over all is to control the transition from laminar to turbulent flow and better match simulations with experiments. To fulfill this aim, different methods can be implemented: the one concerning the PyFR turbulence plugin is referred as synthetic eddy method (SEM). SEMs allow you to inject turbulence in a simulated flow by introducing eddies with a prescribed shape in

the domain: this will lead to the desired fluctuations in the velocity field.

The eddies are generated at $t = 0$ with a uniform distribution within a box positioned wherever in the domain; the section of the box normal to the streamwise direction is defined by the user; then, the solver extrudes this box both upstream and downstream considering the given turbulent length scale, in order to fit at least one eddy in the streamwise width of the box itself. The number of eddies populating the box at $t = 0$ depends on the imposed turbulent length scale.

All the eddies populating the box at the initial time have a random sign and respond to a correlation function R_{ij}, which describes the spatial and time coherence. They are also dependent on a shape function, which is usually a Gaussian: indeed, the σ term shown in the configuration file at section 4, corresponds to the standard deviation of the synthetic eddy profile. Finally, these eddies are convected through the domain by the bulk velocity, which is given to the solver by the user and can be corrected in case of compressibility, using the Mach number. Looking at the set up explored in paragraph 4.2, also density is additionally given to correct the solution in case of compressibility. The turbulence intensity must be given considering the percentage value Tu [%] and the dimension of the turbulent length scale has to be coherent with the dimensionality of the problem. The input parameter "centre" corresponds to the center of the injection plane, which is initially considered as perpendicular to the x-axis; the user has to give the dimensions of this plane along y and z and, finally, if the streamwise direction doesn't coincide with the x-axis, the plane can be rotated by a given angle around a given axis, to be actually perpendicular to the streamwise direction.

Appendix B

Spectral Proper Orthogonal Decomposition [2]

Everything that will be here reported, is authentic to the article by Schmidt O. T. and Colonius T. cited in the appendix title: the interested reader is referred to it for a better understanding.

The Spectral Proper Orthogonal Decomposition (SPOD) is a data driven method used to analyze and postprocess complex datasets, finding a base which can be used to reconstruct the studied field, reducing its dimensions.

As the more known POD, it consists in an eigenvalue problem which can give, in the form of eigenvectors, the above mentioned basis (modes) and, in the form of eigenvalues, the energy of each mode. Ranking these modes considering their energy, it is usually possible to take into account only the most energetic ones and use them to reconstruct the input, with a little loss in the fidelity to reality, but with a considerable gain in terms of complexity reduction (sparsity).

Given this introduction, the mathematical implementation can be described as follows: given a matrix $\mathbf{C}$, kernel of the eigenproblem $\boldsymbol{CW\Phi} = \boldsymbol{\Phi\Lambda}$, the eigenvectors will be stored as columns of the matrix $\boldsymbol{\Phi}$ and the eigenvalues as elements in the diagonal of $\boldsymbol{\Lambda}$ matrix.

The only distinction between the classical POD and the Spectral POD consists

in how the kernel matrix is built: if for the standard POD we have

$$C = \frac{1}{N-1}QQ^H \tag{B.1}$$

with N being the ensemble size, $\mathbf{Q}$ the matrix $M \times N$ containing the dataset variable to be decomposed (M represents the number of observations) and ^{H} the Hermitian, for the SPOD we have that:

$$\hat{C} = \frac{1}{N-1}\hat{Q}\hat{Q}^H \tag{B.2}$$

where $\hat{}$ represents the Fourier transformed value. Hence, the kernel for the SPOD is no more the covariance matrix C but, this time, the CSD matrix $\hat{C}$ (obtained doing the FFT of the covariance matrix itself).

So, looking at the scalar representation of each element of the CSD matrix, we have:

$$\langle \hat{q}_1, \hat{q}_2 \rangle = \int_{\Omega} \hat{q}_1(z)^* W \hat{q}_2(z) dz \tag{B.3}$$

with Ω representing the domain.

Focusing on the implementation, on the context of this work, the SPOD had been performed using the Welch method, which is used to build the CSD matrix from the data, subdividing the time signal into a certain number of segments, or blocks N_{blks}. Each block contains a certain number N_{FFT} of realizations (snapshots) and overlaps with the near segment by a number of $N_{overlap}$ snapshots.

It's important to say that, as the SPOD comes from a Fourier transform of the domain, the CSD matrix $\hat{C}$ is evaluated one frequency at a time.

References

[1] S. Demange, S. Jekosch, B. Church, E. Sarradj, K. Oberleithner, and A. V. Cavalieri, *Experimental investigation of tonal and broadband trailing-edge noise for the flow around a NACA0012 profile with rounded trailing edge.* iv, v, 2, 11, 13, 30, 38, 60

[2] O. T. Schmidt and T. Colonius, "Guide to spectral proper orthogonal decomposition," *AIAA Journal*, vol. 58, no. 3, pp. 1023–1033, 2020. viii, 64

[3] T. Itami, "Basic Course on Turbulence and Turbulent Flow Modeling 10: 10.1 Wall condition of RANS model, 10.2 Wall function, 10.3 Turbulence models and wall condition." `https://www.cradle-cfd.com/media/column/a163`, 2019. Accessed: 2023-11-29. ix, 9

[4] F. Witherden, A. Farrington, and P. Vincent, "Pyfr: An open source framework for solving advection–diffusion type problems on streaming architectures using the flux reconstruction approach," *Computer Physics Communications*, vol. 185, no. 11, pp. 3028–3040, 2014. 2

[5] M. S. J., *Inviscid Incompressible Flow.* Wiley-Interscience, 2001. 4

[6] F. G. K. Batchelor, *AN INTRODUCTION TO FLUID DYNAMICS.* Foundation Books, 2000. 5

[7] B. Mandal and H. Mazumdar, "The importance of the law of the wall,"

International Journal of Applied Mechanics and Engineering, vol. 20, 12 2015. 8

[8] Z. Yuan, S. Demange, S. Jekosch, E. Sarradj, K. Oberleithner, A. Cavalieri, and A. Hanifi, "Wavepackets driving trailing edge noise. (part 1: direct simulation and experiments)," *submitted for AIAA conference*, 2024. 12, 30, 31, 36

[9] M. Drela, "XFOIL: An Analysis and Design System for Low Reynolds Number Airfoils," in *Low Reynolds Number Aerodynamics* (T. J. Mueller, ed.), (Berlin, Heidelberg), pp. 1–12, Springer Berlin Heidelberg, 1989. 14

[10] G. Giangaspero, F. Witherden, and P. Vincent, "Synthetic turbulence generation for high-order scale-resolving simulations on unstructured grids," *AIAA Journal*, vol. 60, no. 2, pp. 1032–1051, 2022. 29, 62